Retrieval of Kinematic Fields Using a Single-Beam Airborne Doppler Radar Performing Circular Trajectories

A. PROTAT, Y. LEMAITRE, AND G. SCIALOM

Centre d'Études des Environnements Terrestre et Planétaires, Velizy, France

(Manuscript received 18 January 1996, in final form 28 November 1996)

ABSTRACT

The present study is devoted to new analyses of single-beam airborne Doppler radar data referred to as SAVAD (single-beam airborne velocity–azimuth display) and double SAVAD. These techniques permit processing of Doppler radial velocities from circular trajectories performed by the aircraft. As in the VAD and double VAD analyses for ground-based radars, these SAVAD and double SAVAD analyses permit diagnosis of crucial mesoscale kinematic and thermodynamic parameters such as the horizontal wind, its horizontal divergence, its stretching and shearing deformations, the vertical air motion, the mean fall velocity of the hydrometeors, the mesoscale vertical vorticity, and horizontal gradients of pressure and temperature perturbations. These analyses are mathematically described. An application of the method to simulated data and to a real dataset extracted from the TOGA COARE database is also presented.

1. Introduction

Previous observational studies on mesoscale precipitating systems, among them squall lines and cold-frontal systems, have demonstrated the importance of stratiform precipitating regions in the dynamics of these disturbances, especially in the interactions between the various scales of motion involved in such systems, in particular through microphysical processes.

These trailing regions of stratiform cloud at the rear of squall lines are found to give an important contribution to the global water budget of the squall lines (Gamache and Houze 1983; Chong et al. 1987; and others) and to be involved in the interaction mechanism responsible for the squall-line regeneration (Zipser 1977; Smull and Houze 1985). Similarly, numerous works evidenced the importance of the rapid growth of these trailing stratiform cloud regions in the intensification of the mesoscale circulation consisting of the familiar rising front-to-rear flow overlaying a downward sloping rear-to-front flow characterizing the mature stage of a squall line. For example, Szeto and Cho (1994) show that the enhanced warming and the precipitation at the rear of the convective line associated with the growth of the stratiform region tend to induce low pressure just behind the convective line in the low to middle levels just below the melting level. The associated pressure gradient forces strengthen the backward updraft to form the rising front-to-rear flow as well as the front portion of the rear-to-front flow. This last flow sinks because of the precipitation loading and cooling effects.

On the other hand, several studies have shown that the diabatic ascending branch of planetary-scale mean tropical circulations is constituted by the tropical convection. As a result, the mean properties of convection, and in particular the vertical heating profiles, have a great impact on weather and climate, which considerably motivates the estimate of vertical mass fluxes within them. As pointed out by Mapes and Houze (1993 and 1995, referred to in the following as MH93 and MH95, respectively), although heating is a fundamental quantity in the thermodynamics, it remains a secondary or derived quantity in observational meteorology that can be quite consistently associated with the horizontal divergence from which these vertical mass fluxes are derived.

The mesoscale vertical vorticity is also an essential quantity to be estimated in order to study the organization and evolution of mesoscale convective systems. For instance, model outputs (Hertenstein and Schubert 1991) using a two-dimensional version of semigeostrophic theory compared with real observations of MCSs suggest that typical features of the profile of potential vorticity anomalies are associated with typical organization and evolution of squall lines. In particular, trailing stratiform regions of precipitation have a strong signature of potential vorticity anomalies in the midtroposphere, while convective lines are characterized by cyclonic flow in the lower levels and anticyclonic flow in the upper troposphere.

Corresponding author address: Dr. Alain Protat, CETP/ABM, UVSQ, 10-12 avenue de l'Europe, Vélizy 78140, France.
E-mail: Alain.PROTAT@cetp.ipsl.fr

Stratiform areas were scrutinized in the past by means of ground-based Doppler radars performing conical scannings using the well-known VAD analysis (velocity–azimuth display) initiated by Lhermitte and Atlas (1961) and improved by Browning and Wexler (1968), Testud et al. (1980), and Srivastava et al. (1986). This method provides vertical profiles of the horizontal divergence of the wind, as well as the horizontal wind itself, its shearing and stretching deformations, and the vertical air motion from conical scannings within stratiform or moderately convective precipitation. Scialom and Testud (1986, referred to in the following as ST86) developed the double VAD (DVAD) analysis using the data from two radars in order to retrieve all the first-order derivatives of the horizontal wind, leading in particular to the determination of the vertical profile of mesoscale vertical vorticity.

The main advantage of these VAD-like analyses, compared to the methods devoted to the three-dimensional wind field retrieval from ground-based radar data, results from the fact that they process a great amount of data in the mesoscale area sampled by the radar, leading to a very good accuracy of the diagnosed kinematic parameters, in particular the vertical air velocity (accurate to within 10 cm s^{-1}) at mesoscale. However, ground-based Doppler radars do not allow a global description of precipitating systems or a study of their evolution since they have insufficient time and space coverage. These limitations have been reduced in the last 10 years with the advent of airborne Doppler radars, which allow (i) observations of the whole precipitating system out of range of land-based radars, especially over the sea, and (ii) quick flights to the storms in order to sample them during their lifetimes.

Thus, in order to produce profiles of the same kinematic parameters as the VAD analysis (in particular the horizontal divergence and vertical vorticity) from airborne Doppler radar data, a new analysis called SAVAD (single-beam airborne velocity–azimuth display) is proposed in the present paper, following the principle of a classical VAD analysis for ground-based radar data. This new method accurately provides the horizontal divergence from airborne radar data in stratiform or moderately convective areas, as well as the stretching and shearing deformations. Moreover, combining results from two airborne radar observations using the DVAD analysis developed for ground-based radar also permits retrieval of the mesoscale vertical vorticity and horizontal gradients of thermodynamic variables (pressure and temperature). The SAVAD analysis is applied to circular paths, also called ''purls'' (see MH95), performed by the airborne Doppler radars. Between two successive straight-flight patterns, the P3-42 aircraft carrying the single-beam radar is often flying a circular path. This has motivated the development of the SAVAD analysis since a VAD approach is geometrically natural to process the data collected during these circular flights. In fact, as shown in section 2b(1), this type of trajectory enables the acquisition of a set of data in a geometry equivalent to that performed by ground-based radars (i.e., conical scannings of vertical axes).

In section 2, the mathematical formulation and the data processing of the SAVAD analysis are described. The accuracies of the retrieved parameters in different simulated cases are discussed in section 3. In particular, we estimated the errors associated with (i) the rather low resolution in azimuth of the airborne radar data during a circular flight, (ii) the hypothesis of a constant radius for the performed circular path, and (iii) the accuracy of the radar pointing angles. An application of this method on a tropical disturbance observed on 15 December 1992 during the TOGA COARE experiment is carried out in section 4. In this section, the kinematic parameters retrieved by applying the simple extension of the DVAD analysis (referred to as double SAVAD) to airborne radar data are compared to those obtained with a more sophisticated technique, devoted to the three-dimensional wind field retrieval, called MANDOP (multiple analytical Doppler; Scialom and Lemaître 1990). Section 5 describes a possible extension of the SAVAD analysis, permitting retrieval of the kinematic parameters from the processing of airborne dual-beam Doppler radar data. Concluding remarks are finally given in section 6.

2. Formulation of the SAVAD methodology

This methodology is an extension to airborne Doppler radar data of the VAD analysis, proposed initially by Lhermitte and Atlas (1961) and improved by Browning and Wexler (1968), Testud et al. (1980), and Srivastava et al. (1986). As in the original VAD analysis, it provides the horizontal wind, its divergence, its stretching and shearing deformations, and an estimate of the mean fall velocity of the hydrometeors at each altitude layer. As explained previously, this analysis is adapted to single-beam radars operating aboard aircraft that fly circular trajectories. In the present case, we used the single-beam radar of the P3-42 aircraft (Jorgensen et al. 1983; Hildebrand and Mueller 1985) performing scannings perpendicular to the track of the aircraft.

The processing of data collected during a circular aircraft path was proposed initially by MH95 using the TOGA COARE dataset. Their approach is based on Stokes's theorem, permitting an accurate retrieval of a mean vertical profile of horizontal divergence by processing all the purls performed during an aircraft mission. In this method, the line integral of the Stokes theorem [see their Eq. (7), in MH95] is evaluated as a discrete sum within a layer 500 m in depth. This discrete sum requires an important number of measurements regularly spaced along the considered horizontal circles. Three independent divergence retrievals using three successive radar range gates are carried out in order to estimate the uncertainty of the retrieval. Moreover, the effect of errors in the imposed hydrometeor fall speed

is minimized by selecting the quasi-horizontal radials in the analysis, even for altitudes far from the flight altitude. An average of all the divergence profiles is then performed considering all the purls of an aircraft mission.

This method differs in many aspects from the analysis described in the present paper. In the SAVAD analysis, the global volume sampled during a single purl is processed in order to retrieve the divergence profile and other crucial kinematic parameters, such as the horizontal wind, its stretching and shearing deformation, the vertical air motion, and the terminal fall velocity of the hydrometeors. These parameters are obtained in layers 300 m in depth in which a great amount of VAD circles is considered in order to minimize the effect of Doppler radial velocity uncertainty. Moreover, in the SAVAD approach, the vertical profiles of horizontal divergence and mean fall velocity of the hydrometeors are retrieved simultaneously through a linear regression allowing a separation of these two parameters [see section 2b(1)]. No assumption is thus carried out for the value of this hydrometeor fall speed.

In this section 2, we will first recall the mathematical formulation of the VAD analysis (section 2a) and then that of the proposed SAVAD approach [section 2b(1)]. Then the specific data processing of the SAVAD analysis will be described in section 2b(2), pointing out the main differences between the VAD and SAVAD analyses.

a. The VAD and DVAD methodologies

The basic hypothesis is the linearity of the horizontal wind, (X_o, Y_o) being the location of the center of the circular aircraft path:

$$U = U_o + U_x(X - X_o) + U_y(Y - Y_o) \quad (1)$$

$$V = V_o + V_x(X - X_o) + V_y(Y - Y_o), \quad (2)$$

which implies that the radial velocity obtained at a particular range gate ρ and for a given elevation α, as a function of the azimuth β, is fully represented by its second-order Fourier series expansion

$$V_r(\beta) = \frac{a_0}{2} + a_1 \cos\beta + b_1 \sin\beta + a_2 \cos(2\beta) + b_2 \sin(2\beta). \quad (3)$$

The five Fourier coefficients a_0, a_1, b_1, a_2, and b_2 are then related to the sampled wind field through

$$a_0 = -\rho \cos^2\alpha \, \mathrm{DIV} + 2V_f \sin\alpha \quad (4)$$

$$a_1 = -V_o \cos\alpha \quad (5)$$

$$b_1 = -U_o \cos\alpha \quad (6)$$

$$a_2 = \frac{1}{2}\rho \cos^2\alpha \, \mathrm{DET} \quad (7)$$

$$b_2 = -\frac{1}{2}\rho \cos^2\alpha \, \mathrm{DES}, \quad (8)$$

where (U_o, V_o) is the horizontal wind at the center of each circle, $V_f = (V_t - w)$ with V_t the mean fall velocity of the hydrometeors (positive downward), and w the vertical air velocity (positive upward). $\mathrm{DIV}(=U_x + V_y)$ is the horizontal divergence, $\mathrm{DET}(=U_x - V_y)$ is the stretching deformation, and $\mathrm{DES}(=U_y + V_x)$ is the shearing deformation. Note that the radial velocity is defined as positive when it is inward (this definition is used throughout the paper).

In practice, a least squares fitting of the Fourier development of the radial winds to the observed ones is performed to obtain the five coefficients. This approach has the advantage of tolerating an irregular data distribution along the circle, provided that there are some measurements in each sector of this VAD circle (see Testud et al. 1980).

The a_1, b_1, a_2, and b_2 coefficients permit direct retrieval of the two components of the horizontal wind, as well as its shearing and stretching deformations. The a_0 coefficient mixes the horizontal divergence and the mean fall velocity of the hydrometeors. In order to separate these terms, three methods can be used: the first one carries out a modeling of V_f by two constants (between 5 and 10 m s^{-1} below the 0°C isotherm and between 0 and 2 m s^{-1} above) and allows a direct determination of DIV from the obtained a_0. The second one consists in estimating the terminal fall speed of the hydrometeors from the radar reflectivity values through an empirical relation $V_f = aZ^b(\rho_o/\rho)^{0.4}$, where Z (mm^6 m^{-3}) is the radar reflectivity, ρ is the air density, and ρ_o is the air density at surface level. The terminal fall speed is more precisely determined with this procedure than with the first one, but the radar reflectivities need to be corrected for attenuation. The third procedure consists of directly estimating these two parameters through a least squares fitting of the a_0 term obtained from each VAD circle at a given altitude layer as a function of the horizontal range (Breger 1977; Matejka and Srivastava 1981), assuming that the vertical air velocity w is weak compared to the hydrometeor fall speed ($V_f \sim V_t$) and minimizing the term

$$\sum_i [Y_i - (-\mathrm{DIV}X_i + V_f)]^2$$

where

$$Y_i = \frac{a_{o_i}}{2 \sin\alpha_i}, \qquad X_i = \frac{\rho_i \cos^2\alpha_i}{2 \sin\alpha_i}. \quad (9)$$

This procedure separates the mean horizontal divergence from the mean fall velocity of the hydrometeors for each altitude. Let us recall that this method is used only when the data collected in the sampling volume contain high-elevation information with a significant projection of the fall velocity included in the radial winds.

The VAD analysis finally provides vertical profiles of U_o, V_o, DET, DES, V_f, and DIV, as well as an estimate

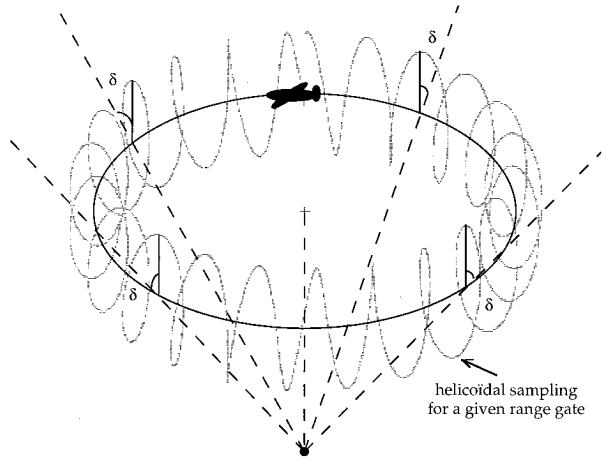

FIG. 1. Helicoidal sampling of the volume during a circular trajectory of the aircraft. The δ angle is the elevation angle with respect to zenith of the cone with vertical axis rebuilt in the new geometry.

of the vertical air velocity, by integrating the airmass continuity equation:

$$w = -\exp\left(\frac{z}{H}\right)\int_0^z \exp\left(-\frac{\zeta}{H}\right)\mathrm{DIV}(\zeta)\,d\zeta, \quad (10)$$

where H is the scale height.

Studies on kinematic structures at the rear of fronts have shown that it was also possible to retrieve the three-dimensional wind field and the mesoscale vertical vorticity with two ground-based Doppler radars (see ST86) using a very simple extension of the classical VAD, called DVAD. Two simultaneous observations of a disturbance with two Doppler ground-based radars are analyzed separately with a simple VAD, and then the results obtained by each of the two radars are combined to retrieve the four first-order derivatives of the horizontal wind field and thus the vertical vorticity ROT($=V_x - U_y$).

b. The SAVAD analysis

As explained previously, the extension of the VAD analysis to the airborne Doppler radar data is based upon geometrical considerations. Let us recall first that the ground-based radar performs conical scans with vertical axes, and the vertices of the cones are always at the radar location, while the airborne radar spins around the track of the aircraft and performs a helicoidal sampling of the volume (see Fig. 1).

To rebuild an equivalent ground-based geometry with the airborne radar data, that is, cones with vertical axis, the aircraft must describe a circular path (see Fig. 2). All these cones intercept this trajectory and each of them is defined by the selected elevation. Thus, selecting radial winds from a given elevation during all the circular trajectory allows us to rebuild one of these cones. Repeating the process for various elevations allows one to obtain all the cones. Note that the location of the vertices of the cones changes along a vertical axis with the selected elevation in the airborne case (see again Fig. 2). In section 2b(1), the mathematical modifications due to these new geometrical considerations are described.

It must be noted, however, that several complications occur beyond those found in the ground-based case that result from the antenna motion in the ground-relative frame. These problems are pointed out in section 2b(2), presenting the processing of the airborne radar data, and the reorganization of these data in the new geometry. Several effects due to the use of airborne radar data must be corrected, in particular the apparent antenna motion must be removed (crucial in the case of a circular path) and the radar pointing angles and ground-relative velocity of the aircraft must be accurately corrected (see appendix A). Another major complication results from the azimuthal resolution of the single-beam radar onboard the aircraft, which is 10 times less than that of the ground-based case [section 2b(2)].

1) MATHEMATICAL FORMULATION

As in the VAD analysis, the horizontal wind in the SAVAD analysis is assumed to vary linearly. This leads to a second-order Fourier development of the radial wind whose coefficients can be written as

$$a_0 = -\rho\cos^2\alpha\ \mathrm{DIV} - \boldsymbol{R_c\cos x\cos\alpha\ DIV} + \boldsymbol{R_c\sin x\cos\alpha\ ROT} + 2V_f\sin\alpha \quad (11)$$

$$a_1 = -V_o\cos\alpha \quad (12)$$

$$b_1 = -U_o\cos\alpha \quad (13)$$

$$a_2 = \frac{1}{2}\rho\cos^2\alpha\ \mathrm{DET} + \frac{\mathbf{1}}{\mathbf{2}}\boldsymbol{R_c\cos x\cos\alpha\ DET} + \frac{\mathbf{1}}{\mathbf{2}}\boldsymbol{R_c\sin x\cos\alpha\ DES} \quad (14)$$

$$b_2 = -\frac{1}{2}\rho\cos^2\alpha\ \mathrm{DES} - \frac{\mathbf{1}}{\mathbf{2}}\boldsymbol{R_c\cos x\cos\alpha\ DES} + \frac{\mathbf{1}}{\mathbf{2}}\boldsymbol{R_c\sin x\cos\alpha\ DET}, \quad (15)$$

where x is the horizontal angle between the vertical plane perpendicular to the circular trajectory at a given location and the vertical plane defined by the direction pointed by the antenna (illustrated Fig. 3), $V_f(=V_t - w)$, where V_t is the mean fall velocity of the hydrometeors (positive downward), w is the vertical air motion (positive upward), and R_c is the mean radius of the purl. The determination of this radius R_c and its standard deviation are performed during the preprocessing of the airborne radar data. It allows us to check the quality of the purls that have been carried out.

The terms in boldface represent the additional terms that appear in the airborne case. Notice in particular that

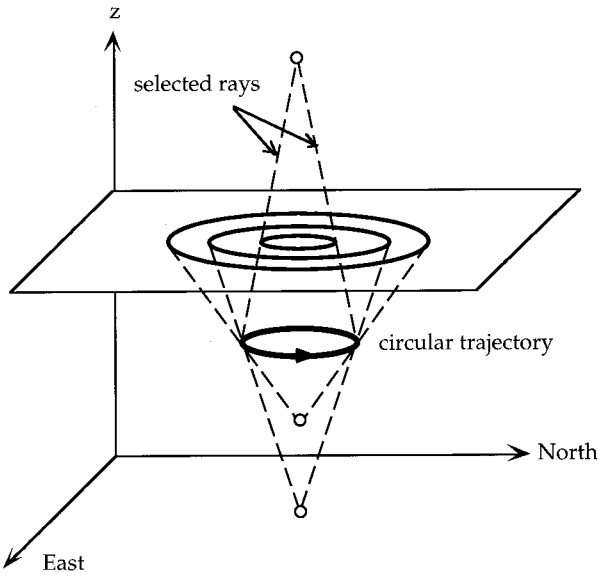

FIG. 2. Illustration of the different contributions of the cones on a considered horizontal plane during a circular flight.

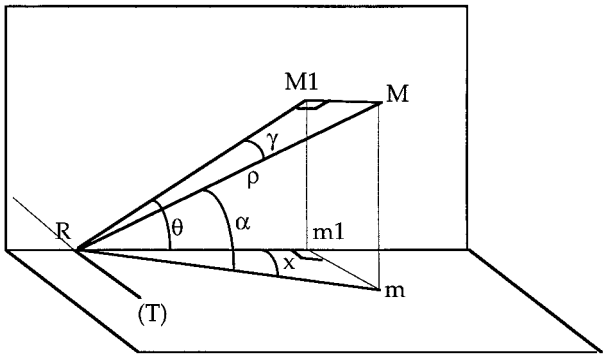

FIG. 3. Definition of the angles and range gates: *RM* is the direction of the considered sample, *Rm* is its projection on the horizontal plane at the altitude of the aircraft. The vertical plane *RM*1*m*1 is perpendicular to the circular trajectory of the aircraft at the location *R*; (*T*) represents the tangent to this circular trajectory; α is the earth-relative elevation angle; θ is the elevation of the projection of the Doppler radial on the vertical plane (*RM*1*m*1); γ is the ''elevation'' of the Doppler radial from the plane (*RM*1*m*1) perpendicular to the track; *x* is the projection of γ on the horizontal plane; and ρ is the range gate.

the horizontal divergence is now mixed with the vertical vorticity in the first equation when the *x* angle is not negligible. In the SAVAD approach, which is devoted to the processing of the single-beam radar data from the NOAA P3-42 single-beam antenna performing occasional scannings nearly perpendicular to the trajectory of the aircraft (FAST mode generally), *x* is close to 0. In fact, this angle, referenced to the ground reference frame, slightly varies due to the antenna motion itself and to the fluctuations of the aircraft navigation angles (essentially the drift angle) along the circular trajectory.

Let us calculate the maximum *x* angle tolerated by the SAVAD analysis. It corresponds to the condition that the additional terms depending on the angle *x* can be neglected, that is,

$$|\rho \cos^2\alpha \text{ DIV} + R_c \cos x \cos\alpha \text{ DIV}| \gg |R_c \sin x \cos\alpha \text{ ROT}|, \quad (16)$$

which can be rewritten

$$|(\rho \cos\alpha + R_c \cos x)\text{DIV}| \gg |R_c \sin x \text{ ROT}|. \quad (17)$$

Taking $\rho = 0$ to reduce the tolerance on *x* leads to

$$|\tan(x)| < 0.1\frac{\text{DIV}}{\text{ROT}}. \quad (18)$$

From Fig. 3, we can show that

$$\sin\gamma = \cos\alpha \sin x. \quad (19)$$

The maximum elevation angle α_m that can be used in the processing is then a function of *x* and γ, *x* being itself a function of DIV and ROT [see (18)]. Calculation of averages and standard deviations of γ for the TOGA COARE purls has shown that typical values of γ were found between $-0.1°$ and $0.1°$, with a standard deviation of $\pm 1°$.

For DIV $\sim$ ROT, then $x < 6°$ [see Eq. (18)], which leads to $\alpha_m \sim 80°$ [see Eq. (19)]. For DIV $\sim$ ROT/4, then $x < 1.4°$, and $\alpha_m \sim 45°$.

We can see that in ''extreme cases,'' that is, when DIV ~ 0 and ROT $\neq 0$, no solution is found for α_m. Nevertheless, since a great amount of VAD circles is considered in this processing, the impact of these raw data is found to be weak, as it can be seen in the simulations of section 3 (see the quality of the retrieval for given altitudes where DIV ~ 0 and ROT $\neq 0$), and the SAVAD analysis can be applied, the error on the kinematic parameters increasing as the number of extreme cases increases. Moreover, it must be noted that we made the present discussion for $\rho = 0$, which reduces considerably the tolerance on *x*. When ρ increases, the condition on DIV/ROT can be relaxed, and then greater values for *x* and α_m can be tolerated. We have chosen, however, to limit the elevation to 60° in order to minimize this problem, even if it was possible to keep data of higher elevation in the processing.

Under these conditions, the coefficients of the second-order Fourier development can be written

$$a_0 \sim -(\rho \cos\alpha + R_c) \cos\alpha \text{ DIV} + 2V_f \sin\alpha \quad (20)$$

$$a_1 = -V_o \cos\alpha \quad (21)$$

$$b_1 = -U_o \cos\alpha \quad (22)$$

$$a_2 \sim \frac{1}{2}(\rho \cos\alpha + R_c) \cos\alpha \text{ DET} \quad (23)$$

$$b_2 \sim -\frac{1}{2}(\rho \cos\alpha + R_c) \cos\alpha \text{ DES}. \quad (24)$$

These coefficients appear very similar to those obtained with the VAD analysis. The main difference comes from the horizontal distance from the center of the circles that now includes the mean radius of the purl. Since this distance is supposed constant, the accuracy of the a_0, a_2, and b_2 coefficients will depend on the quality of this hypothesis. This accuracy will be estimated in the following for the TOGA COARE data (see section 3b). Note here that the least squares fitting allowing to separate in the term a_0 the horizontal divergence from the mean fall velocity of the hydrometeors in the classical VAD analysis can be done by one of the following procedures.

The first procedure consists in rewriting (20) under the form

$$\frac{a_0}{2\ \sin\alpha} = \frac{-\mathrm{DIV}}{2h}\rho_h^2 - \frac{R_c\ \mathrm{DIV}}{2h}\rho_h + V_f, \qquad (25)$$

where $\rho_h = \rho\ \cos\alpha$ is the horizontal range from the aircraft and $h = \rho\ \sin\alpha$ is the altitude with respect to the aircraft. This leads to a quadratic regression.

Rewriting (25) under the form

$$\frac{a_0}{2\ \sin\alpha} = -\mathrm{DIV}\left(\frac{\rho_h^2 + R_c\rho_h}{2h}\right) + V_f \qquad (26)$$

leads to a second procedure, consisting in a simple linear regression:

$$\sum_i [Y_i - (-\mathrm{DIV}X_i + V_f]^2 \text{ minimum}$$

with

$$X_i = \frac{\rho_h^2 + R_c\rho_h}{2h}, \qquad Y_i = \frac{a_{0_i}}{2\ \sin\alpha_i}. \qquad (27)$$

This latter procedure (carrying out the simple linear regression) has been chosen for accuracy considerations. We can show effectively that the associated errors on DIV and V_f are weaker in this latter case.

As will be shown in section 3, these errors on V_f increase when the number of measurements along the circles decreases. This degraded resolution implies in particular that the linear regression permitting retrieval of DIV and V_f is in turn degraded by greater errors on the a_0 terms. In order to minimize this problem, the a_0 coefficients resulting from the first step of the processing are now weighted by the inverse of their variance in the linear regression.

The accuracy of DIV and V_f in the linear regression of (27) with weighting factors σ_i can be written as

$$\sigma^2_{\mathrm{DIV}} = \frac{1}{\Delta}\sum_i (\sigma_i^2)$$

$$\sigma^2_{V_f} = \frac{1}{\Delta}\sum_i (\sigma_i^2 X_i^2) \qquad (28)$$

with

$$\Delta = N\sum_i X_i^2 - \left(\sum_i X_i\right)^2,$$

where

$$\sigma_i^2 = \frac{\sigma^2(a_{0_i})}{4\ \sin^2\alpha} = \frac{\sigma^2(V_r)}{8N_i\ \sin^2\alpha}. \qquad (29)$$

Here $\sigma(V_r)$ is the instrumental standard deviation on radial velocities (approximately 1 m s^{-1} for the P3 systems), and N_i is the number of measurements on the ith VAD circle. Note that when α tends to 0, the error on V_f strongly increases [see (28) and (29)]. To minimize this problem, the measurements corresponding to elevations between $-0.25°$ and $0.25°$ have been systematically removed during the data preprocessing.

Section 2b(2) aims at presenting the processing of the airborne radar data and the improvements carried out for minimizing in particular the impact of the rather low azimuthal resolution of airborne radar data during a circular path.

2) The specific processing for the SAVAD analysis

Before using the SAVAD analysis, a first step of preprocessing is necessary to correct data from several effects. The different corrections carried out in this preprocessing of the airborne Doppler radar data are presented in appendix A.

The main new element that has to be pointed out for the preprocessing of the data collected during a circular aircraft path is the removal of the apparent antenna motion (Lee et al. 1994). As explained in appendix A, the associated potential radial wind bias that has been observed during circular flights of TOGA COARE was approximately 1.5 m s^{-1}. Note also that this bias would have been very damaging on the retrieval of the horizontal divergence and the vertical vorticity of the wind if not corrected.

Once these corrections have been carried out, a consistent dataset can be analyzed. Let us now introduce the specific processing of the airborne radar data for the application of the SAVAD analysis.

The main difference between the ground-based and airborne cases is the azimuthal resolution obtained for each circle in each horizontal plane: for the P3 systems, the antenna carries out a 360° rotation in approximately 6 s. If the aircraft has a velocity of 130 m s^{-1} and performs a 5-km-radius circular trajectory, which are realistic assumptions, the horizontal angular resolution is approximately 10°. It means there is only one radial wind every 10° along each VAD circle, which is quite a bad resolution compared to that obtained in the ground-based case (approximately 1°).

It is then preferable to process purls with more than a single turn of the aircraft. In the TOGA COARE dataset, circular trajectories of one-and-one-half turns are

often performed, and we have noticed significant improvements (not shown here) in the results obtained with the SAVAD analysis.

It must be noted here that a system such as the ELDORA–ASTRAIA facility (Electra Doppler Radar-Analyse Stéréoscopique par Radar à Impulsions Aéroporté; Hildebrand et al. 1995) will provide in the near future a better azimuthal resolution thanks to its faster antenna rotation.

The corrected airborne radar data are then relocated in a typical geometry of ground-based radars, that is, conical scannings of vertical axis (see Fig. 2), using grid points defined by 0.5° in elevation, 1° in azimuth (although a real sampling only provides one value each 10° along the circles), and a 300-m range gate. This configuration permits a sufficient filling of the individual VAD circles from which each set of Fourier coefficients ($a_0, \ldots, b_2$) is estimated and corresponds to a satisfying computing time. Moreover, as explained previously, the elevation angle is limited to 60°, so that the angle γ be accurate to within 3° [as described in section 2b(1)], and measurements at elevations between $-0.25°$ and 0.25° are removed since they are affected by greater errors.

3. Simulations

This section evaluates the errors in parameters retrieved by the SAVAD analysis, that is, the horizontal wind, its horizontal divergence, its shearing and stretching deformations, and the mean fall velocity of the hydrometeors. For these purposes, a linear horizontal wind field is constructed, ensuring that the first-order horizontal derivatives are constant.

The vertical air velocity w is neglected with respect to the mean fall speed of the hydrometeors since previous studies have shown that the contribution of w compared with that of the divergence in the a_0 term [see (20)] never exceeds 10% (see Scialom and Lemaitre 1994). Note that all these simulations include the corrections described in appendix A, permitting an overall verification of the preprocessing step.

The influence of the azimuthal resolution on the retrieval of these parameters is particularly discussed in section 3a. In section 3b, the simulation is carried out to test the hypothesis of a constant radius of the purl in the SAVAD analysis by building the radial winds with purls characterized by a non–strictly constant radius. The kinematic parameters are then retrieved considering that this radius is constant. The impact of an addition of a little quadratic component to the horizontal wind is also evaluated in the case of this imperfectly flown circle.

In section 3c, a simulation of two self-consistent horizontal wind fields associated with two spaced circular trajectories is carried out to estimate the errors in the four first-order derivatives of the horizontal wind field retrieved by the double SAVAD analysis. This allows the retrieval of all the derivatives and thus of the vertical vorticity and of the three-dimensional wind field.

Section 3d describes the simulation of a systematic error on the radar navigation angles so as to evaluate the associated errors for the kinematic parameters. This simulation is carried out using a real data filling deduced from the TOGA COARE dataset. Note that all the errors presented in this section 3 are estimated as in (28) of section 2b(1) and that the details of all the simulated wind fields of this section are described in appendix B.

a. Influence of the azimuthal resolution and data filling on the kinematic parameters accuracy

The purpose of this section is to describe the effect of the poor azimuthal and radial resolution on the accuracy of the kinematic parameters retrieved by the SAVAD analysis. For this purpose, three different simulations are carried out, with addition of a Gaussian noise 1 m s^{-1} standard deviation to the radial wind, corresponding approximately to the noise of the airborne P3 radar data.

We have simulated a wind field consistent with the characteristics of disturbances observed during TOGA COARE and deduced from previous studies (MH93) and from our own retrievals. Details of this simulation (referred to as type I) are given in appendix B.

The first simulation consists in creating a 1° azimuthal resolution, with a complete filling of data along the rays. The second simulation is equivalent to the first one, but with a 10° azimuthal resolution. The third one is performed considering a real dataset, but replacing the measured radial velocities by the simulated ones. This procedure reduces again the number of measurements in the VAD circles.

Using a 1° azimuthal resolution and a Gaussian noise 1 m s^{-1} standard deviation added to the radial wind, the SAVAD analysis provides the parameters of the horizontal wind and the mean fall velocity of the hydrometeors with the following errors:

$$\delta(U_o) \approx \delta(V_o) \approx 0.02 \text{ m s}^{-1}$$

$$\delta(\text{DIV}) \approx \delta(\text{DET}) \approx \delta(\text{DES}) \approx 3 \times 10^{-7} \text{ s}^{-1}$$

$$\delta(V_f) \approx 0.01 \text{ m s}^{-1}.$$

The simulations carried out for the case of the classical VAD applied to ground-based radar data gave the same results for the horizontal wind (Scialom and Lemaître 1994) with the same Gaussian noise. It is to be noticed also that the error on the estimate of the mean fall velocity is small.

When the azimuthal resolution is fixed to 10°, the errors on the retrieved parameters become

$$\delta(U_o) \approx \delta(V_o) \approx 0.06 \text{ m s}^{-1}$$

$$\delta(\text{DIV}) \approx \delta(\text{DET}) \approx \delta(\text{DES}) \approx 1 \times 10^{-6} \text{ s}^{-1}$$

$$\delta(V_f) \approx 0.03 \text{ m s}^{-1}.$$

These errors are found to be three times greater than in the first simulation, consistent with 10 times less data, but they still remain satisfying. This increase of the error on DIV and V_f can be easily understood considering the performed linear regression on each horizontal plane to separate DIV and V_f [see (28)].

Since the number N of points simulated in each circle is smaller (see Figs. 4a and 4b), the uncertainty on the a_{o_i} terms [$\sigma^2(a_{o_i}) = \sigma^2(V_r)/2N$] increases. This implies that the slope and the Y-axis intercept related to DIV and V_f are in turn less precisely determined. This effect on DIV and V_f is strengthened when the number of points is again reduced in the third simulation, that is, when considering a real sampling (see Fig. 4c). The typical values of the errors associated with this last simulation are then found to be

$$\delta(U_o) \approx \delta(V_o) \approx 0.1 \text{ m s}^{-1}$$

$$\delta(\text{DIV}) \approx \delta(\text{DET}) \approx \delta(\text{DES}) \approx 2 \times 10^{-6} \text{ s}^{-1}$$

$$\delta(V_f) \approx 0.04 \text{ m s}^{-1}.$$

In summary, these simulations have permitted an estimate of the typical accuracy of the kinematic parameters retrieved by the SAVAD analysis and evidence of the azimuthal resolution's influence on the errors associated with these parameters.

It must be noted that in all the previous simulations, the presented errors are averaged values that do not depend on the considered height. In fact, we can show in particular from (29) that the error on V_f increases while the elevation angle α decreases; that is, the maximum error occurs at the altitude of the aircraft. This point is evidenced in the application on real data in section 4.

Let us recall also that only a 10° azimuthal resolution can be expected from the P3 systems and that in future international projects the ELDORA–ASTRAIA system will be able to perform a better resolution with its faster antenna rotation.

b. Influence of the mean radius accuracy on the estimate of the kinematic parameters

The mean radius of the performed purl is estimated in the preprocessing, as well as its standard deviation. For the TOGA COARE purls, this mean radius was approximately 5 km, with a standard deviation oscillating from 0.2 to 1 km. In practice, a better accuracy of the retrieved kinematic parameters is clearly obtained when the circularity of the trajectory is excellent.

In fact, let us recall that in the SAVAD analysis the radius of the circular aircraft path considered in (20), (23), and (24) is assumed to be constant and corresponds to the mean radius of the purl estimated in the preprocessing step. Thus, in the processing, the standard deviation on this quantity is not taken into account.

This assumption is tested in the following using the same procedure as in the third simulation of section 3a,

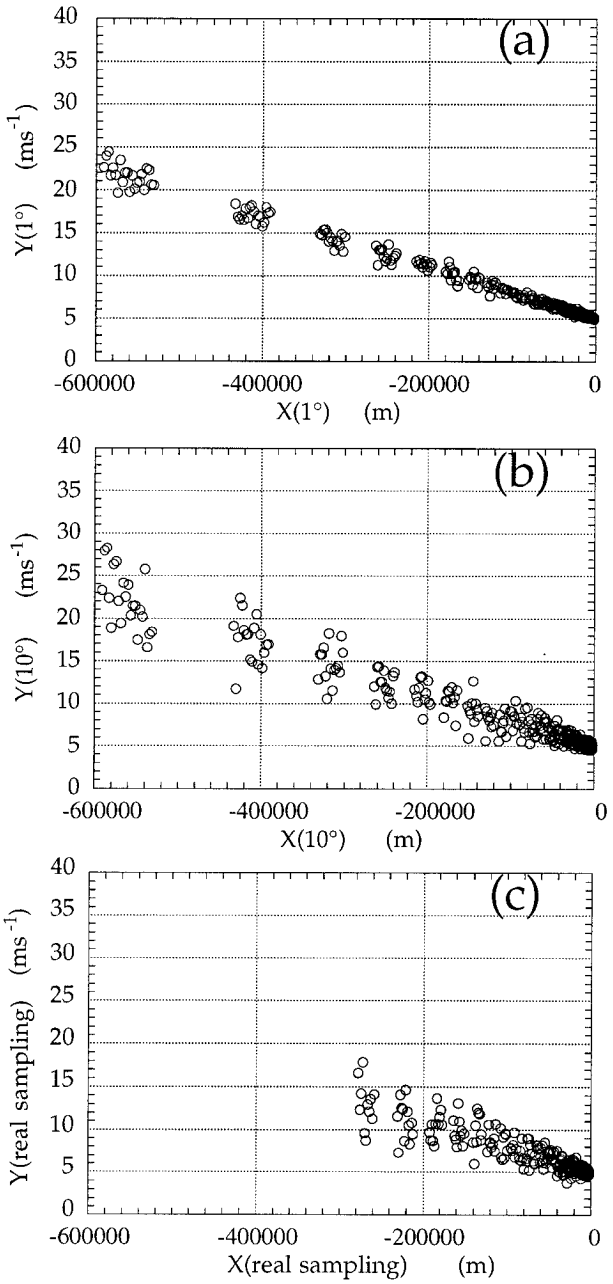

FIG. 4. Least squares fittings on X and Y [$X = (\rho_h^2 + R_c\rho_h)/2h$ and $Y = a_0/(2 \sin\alpha)$, see Eq. (27), section 2b(1)] allowing separation of the horizontal divergence and the terminal fall velocity of the hydrometeors for a given horizontal plane $z = 1950$ m (a) when the azimuthal resolution is 1°, (b) when the azimuthal resolution is 10°, and (c) when considering a real data filling and replacing the real radial velocities by the simulated ones.

that is, replacing in a real dataset the real radial velocities by the simulated ones. These radial velocities are now simulated through the five Fourier coefficients of (20)–(24), but replacing R_c by $R_c = R_{co} + A \cos(8\beta)$ in the calculation of the a_0, a_2, and b_2 coefficients, A being the standard deviation of the radius. The purl becomes

in this simulation an elliptical path. A Gaussian noise 1 m s^{-1} standard deviation is then added to the obtained radial velocities. The values of the simulated horizontal wind and first-order derivatives are the same as in section 3a.

The mean radius R_{co} (instead of R_c) is then introduced in the SAVAD analysis to retrieve the five Fourier coefficients from which the kinematic parameters are deduced.

For $A = 0.2$ km, we have noticed that the errors were approximately the same as for the third simulation of section 3a. This implies that the error associated with only the effect of the mean radius of the purl is negligible with respect to the other errors.

For $A = 1.0$ km, these errors become

$$\delta(U_o) \approx \delta(V_o) \approx 0.2 \text{ m s}^{-1}$$

$$\delta(\text{DIV}) \approx \delta(\text{DET}) \approx \delta(\text{DES}) \approx 4 \times 10^{-6} \text{ s}^{-1}$$

$$\delta(V_f) \approx 0.07 \text{ m s}^{-1}.$$

These errors are still satisfying. Another kind of imperfectly flown circles has also been considered, corresponding to a global drift of the aircraft during the aircraft path. For the TOGA COARE purls, we found a typical value of the horizontal displacement X_d due to the drift of about 2 km. This corresponds to a 7 m s^{-1} advection in the ground-relative frame for a 5-min purl.

Considering a 7 m s^{-1} advection, and also a stronger value of 10 m s^{-1} corresponding to $X_d = 3$ km, we found that the associated errors were the same as those obtained when considering an elliptical path with a standard deviation of $A = 1$ km. We can then conclude that the hypothesis of a constant radius in the Fourier equations (20), (23), and (24) does not have a strong influence on the retrieval, provided that the standard deviation on the radius of the circle does not exceed 25% of this radius.

It is also interesting to test the performance of the SAVAD analysis when a little quadratic component is added to the horizontal wind in the case of this imperfectly flown circle defined by $A = 1.0$ km. The simulation of this quadratic wind field is described in appendix B (simulation type II).

Taking $U_{xx} = U_{yy} = 6 \times 10^{-9}$ m^{-1} s^{-1} (which corresponds to a 1.2 m s^{-1} contribution to the horizontal wind at 10 km far from the aircraft while the DIV value of 3×10^{-4} s^{-1} leads to 3 m s^{-1} at this range) leads to approximately the same errors as those found without the quadratic component, which is very satisfying.

For $U_{xx} = U_{yy} = 1 \times 10^{-8}$ m^{-1} s^{-1} (which corresponds this time to a 2 m s^{-1} contribution to the horizontal wind at 10 km far from the aircraft), these errors become

$$\delta(U_o) \approx \delta(V_o) \approx 0.4 \text{ m s}^{-1}$$

$$\delta(\text{DIV}) \approx 7 \times 10^{-6} \text{ s}^{-1}$$

$$\delta(\text{DET}) \approx \delta(\text{DES}) \approx 1.2 \times 10^{-5} \text{ s}^{-1}$$

$$\delta(V_f) \approx 0.15 \text{ m s}^{-1}.$$

Finally, when greater values of this quadratic component are introduced (typically more than 1.5×10^{-8} m^{-1} s^{-1}), significant degradation occurs, which implies that, in this case, the Fourier development must be expanded up to order 3 to retrieve the kinematic parameters [see the QVAD analysis developed by Scialom and Lemaître (1994)]. However, we can see that if the quadratic component is not too strong, the retrieval is still accurately performed.

c. *Accuracy of the first-order derivatives retrieved by the double SAVAD analysis*

As previously noticed, the SAVAD analysis can be applied separately for two spaced purls and analyzed simultaneously in a double SAVAD analysis for airborne radars equivalent to the DVAD analysis (ST86) for ground-based radars. It allows the retrieval of the four first-order derivatives of the horizontal wind, from which the three-dimensional wind field and the mesoscale vertical vorticity ROT are rebuilt. As for the previous simulations, these four first-order derivatives are assumed to be constant, and the vertical air velocity is negligible. A Gaussian noise 1 m s^{-1} standard deviation is added to the radial velocities, and a 10° azimuthal resolution is still chosen.

The aim of this subsection is to test the applicability of this double SAVAD procedure. For this purpose, we considered two circular trajectories spaced 50 km apart in the east direction and 50 km in the north direction. As previously noted, the first-order derivatives and the values of the horizontal wind at the center of each trajectory are chosen in order to fit a real case study. Details of this simulation type III are given in appendix B.

The corresponding profiles of horizontal divergence, stretching, and shearing deformations are given in Figs. 5a, 5b, and 5c, respectively, as well as the kinematic parameters retrieved by the SAVAD analysis applied to each of the two purls. We notice there is a good agreement between the simulated and retrieved values, as expected from the previous simulations, the errors on these parameters being of the same order of magnitude.

The principle of the second step, following ST86, consists in separating the four first-order derivatives of the horizontal wind from the horizontal divergences, shearing, and stretching deformations previously retrieved by the SAVAD analysis. In fact, the SAVAD analysis provides both the horizontal divergence ($U_x + V_y$) and the stretching deformation ($U_x - V_y$) from which we can separate U_x and V_y and the shearing deformation depending on U_y and V_x. Nevertheless, this single relation between U_y and V_x is insufficient for separating in the SAVAD analysis these two derivatives. In the double SAVAD approach, it becomes possible to separate them from the combination of two purls and thus to rebuild the mesoscale vertical vorticity ($V_x - U_y$) and the three-dimensional wind field. The hypothesis is that

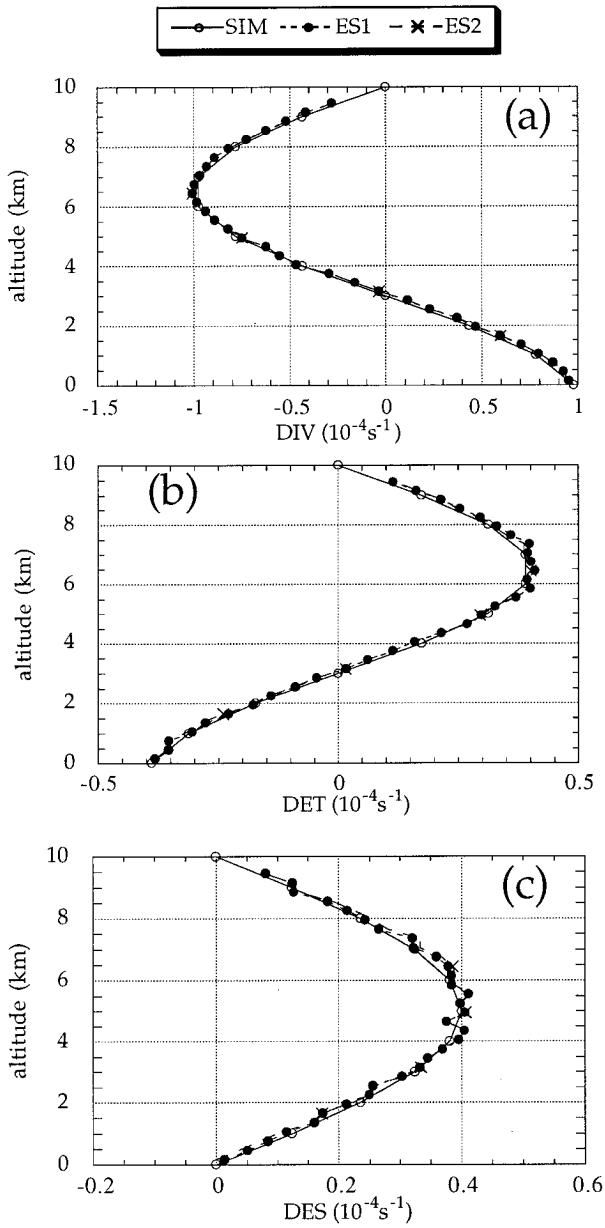

FIG. 5. Comparison of the simulated (SIM) and retrieved values of (a) horizontal divergence DIV, (b) stretching deformation DET, and (c) shearing deformation DES. For each parameter, the two estimates denoted (ES1) and (ES2) correspond to the results of the two simulated circular trajectories necessary for the application of the double SAVAD analysis. All these parameters are expressed in 10^{-4} s^{-1}.

the derivatives deduced from the two estimates are identical. This assumption is checked a posteriori.

Figures 6a, 6b, 6c, and 6d show the accuracy of this double SAVAD analysis. We can notice in particular that the U_y and V_x derivatives that allow us to rebuild the mesoscale vertical vorticity ROT ($=V_x - U_y$) are well from the retrieved two estimates of the shearing deformation. When calculating the standard deviation on these first-order derivatives of the horizontal wind, values between 0.8×10^{-6} and 1.5×10^{-6} are found. They are of the same order of magnitude as the previous estimated errors on the kinematic parameters depending on these derivatives, that is, the horizontal divergence and the shearing and stretching deformations.

d. Influence of the navigation angles accuracy

In this section, systematic errors on the navigation angles of the aircraft, that is, pitch, drift, and roll angles (see Fig. 7), are simulated in order to estimate their influence on the retrieved kinematic parameters. Let us notice that these errors also directly degrade the accuracy of the radar pointing angles. In this simulation, all the steps of the preprocessing described in appendix A are taken into account. For this purpose, the wind is simulated at the beginning of the preprocessing of a real sampling deduced from TOGA COARE, which means again that only the radial velocities are simulated. The parameters chosen for this simulation type IV are described in appendix B.

The simulation consists of adding a systematic error of 1° separately to each of the three navigation angles. This error is introduced in the preprocessing, when calculating the earth-relative radar pointing angles (α and β defined in section 2a) from the aircraft-relative radar pointing angles [see Lee et al. (1994) for the transformation matrices of rotation associated with the roll, pitch, drift, and track angles]. This 1° value is greater than the error that is expected from the airborne radars, especially when using the procedure to correct for navigation errors proposed by Testud et al. (1995). Moreover, it is to be noted that in the case of real Doppler radar data, these errors are not systematic, but fluctuating, and would be filtered out by the linear regression used in this analysis. For each case, the parameters retrieved by the SAVAD analysis with and without addition of errors on each navigation angle are compared.

The obtained results show that an error of 1° on the roll angle has the most significant influence on the estimate of the parameters since it creates a vertical offset on DIV, DET, and DES (see the curves corresponding to the roll angle in Figs. 8a, 8b and 8c, respectively) and an error of approximately 0.5 m s^{-1} on the V_o component of the horizontal wind (not shown), whereas an error of 1° on the pitch and drift angles produces weaker errors (see the same figures and the curves corresponding to the pitch angle).

The vertical offset due to the roll angle is found to be approximately −500 m, which gives maximum errors of approximately 2×10^{-5} s^{-1} for DIV, DET, and DES and 0.5 m s^{-1} for the horizontal wind when considering a horizontal plane. Nevertheless, when adding a more realistic 0.2° error to the roll angle, errors are less than 5×10^{-6} s^{-1} (Fig. 9a) for the horizontal divergence and the shearing and stretching deformations.

Systematic errors that could occur are now corrected

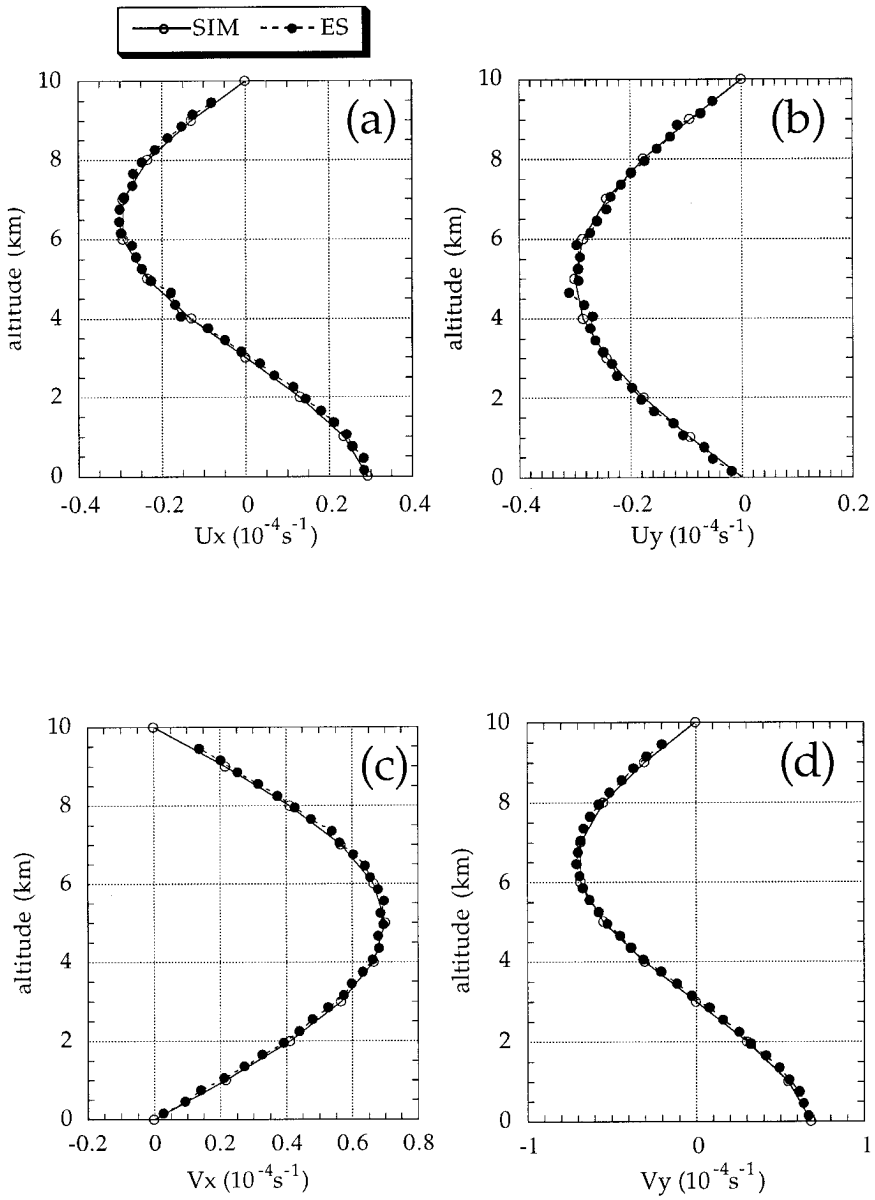

FIG. 6. Comparison of the simulated (SIM) and retrieved (ES) values of (a) U_x, (b) U_y, (c) V_x, and (d) V_y deducted from the double SAVAD analyzis. All these derivatives are expressed in 10^{-4} s^{-1}.

in the preprocessing of the airborne Doppler radar data using the echo returned from the earth's surface (Testud et al. 1995). Thus, the only remaining errors on the navigation and radar pointing angles are reduced to fluctuating errors. In this context, the last simulation consists in adding to the roll angle a Gaussian noise 0.2° standard deviation. The results (only the horizontal divergence is presented Fig. 9b) are in a good agreement with the simulated values. The errors are in this case less than 3×10^{-6} s^{-1}, which evidences that the retrieval of the kinematic parameters is not strongly dependent on a simulated error in the navigation angles.

4. Application to real data

In this section, the SAVAD and double SAVAD analyses are applied on a real airborne dataset collected during the intensive observing period (IOP) of TOGA COARE. This IOP took place from 1 November 1992 through 28 February 1993 in the western equatorial Pacific Ocean region.

The scientific goals of the TOGA COARE experiment defined by Webster and Lukas (1992) are to describe and understand (i) the principal atmospheric processes that organize convection in the warm-pool region, (ii) the principal processes responsible for coupling of the

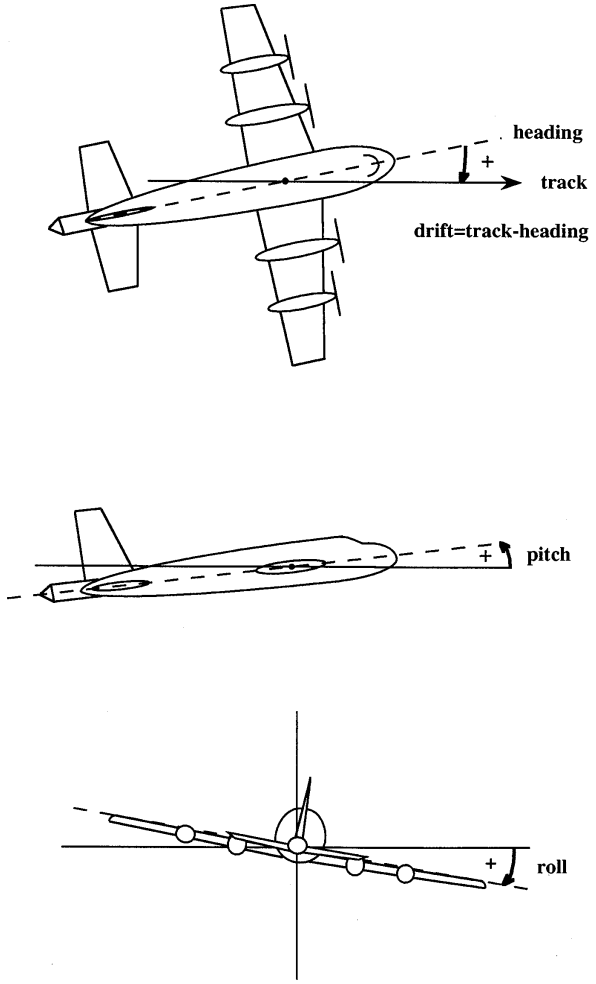

FIG. 7. Definitions of the pitch, drift, and roll angles in the aircraft coordinate system.

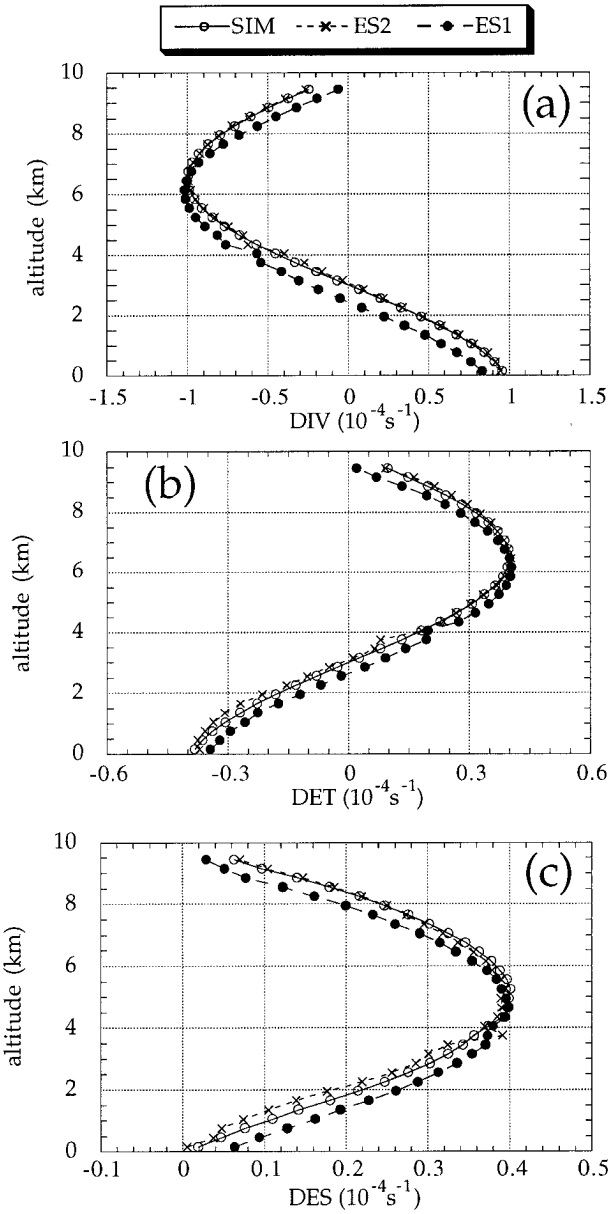

FIG. 8. Comparison of simulated (SIM) and retrieved values of (a) horizontal divergence DIV, (b) stretching deformation DET, and (c) shearing deformation DES, when adding a systematic error of 1° on the roll angle (ES1) or on the pitch angle (ES2).

ocean and the atmosphere in the western Pacific warm-pool system, (iii) the oceanic response to combined buoyancy and wind stress forcing in the western Pacific warm-pool system, and (iv) the multiple-scale interactions that extend the atmospheric and oceanic influences of the western warm pool systems to other regions, and vice versa.

The most spatially extended tropical mesoscale convective system sampled during TOGA COARE was observed on 15 December 1992. The two NOAA P3 aircraft flights collected continuous information about this disturbance from 1700 to 2100 UTC. Eight complete purls have been performed during the P3-42 flight in different regions of the precipitating system.

This MCS is characterized by a region more or less stratiform on the northwestern part and a narrow region of strong precipitation oriented northeast–southwest located ahead and southeast of this stratiform area. The reflectivity trough is not embedded between the two previous regions as is typical but is located on the northeastern part of the global system. This gives this case study its interesting three-dimensional aspect. The detailed description of this MCS and the interpretation of its development and organization in terms of multiple-scale interactions is currently under progress using the MANDOP and SAVAD analyses and the ECMWF (European Centre of Medium-Range Weather Forecasts) model outputs.

In this section, the results obtained from the processing by the SAVAD analysis of two circular trajectories performed on 15 December 1992 are presented in section 4a. The kinematic parameters deduced from

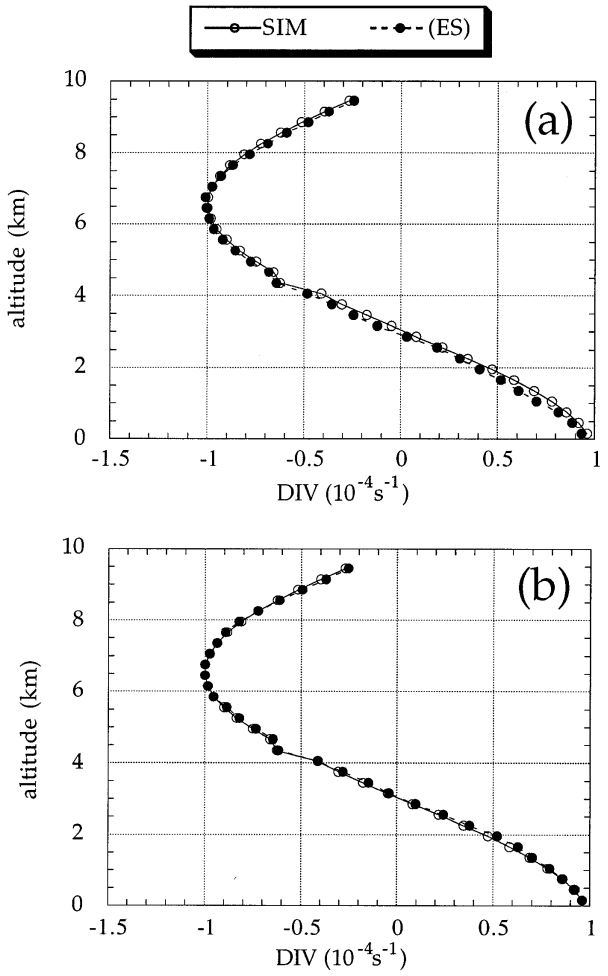

FIG. 9. Comparison of simulated (SIM) and retrieved (ES) values of the horizontal divergence when adding (a) a systematic error of 0.2° or (b) a Gaussian noise 0.2° standard deviation to the roll angle.

the double SAVAD analysis applied to this dataset are also compared in section 4b to those obtained independantly with the MANDOP analysis applied to the same region.

a. Application of the SAVAD analysis on the 15 December 1992 MCS

A time-composite reflectivity map of the lower fuselage radar on board the P3-42 aircraft is shown in Fig. 10, as well as the trajectory of the aircraft from 2025 to 2100 UTC. The circular trajectory located on the western part of the domain is the 2040 UTC purl. The other two at 2025 and 2055 UTC are the purls used to process the SAVAD analysis. The vertical profiles of mean reflectivity at 2025 and 2055 UTC (Fig. 11d) deduced from the SAVAD analysis show a typical feature of stratiform regions: an increase of the reflectivity (expressed in dB*Z*) in the rain region, a signature of the bright band, and a decrease above.

The results obtained with SAVAD and double SAVAD applied on the 2025 and 2055 UTC purls are presented together for each of the kinematic parameters in order to compare them and to test the linear hypothesis used in the methodology (i.e., the horizontal constancy of the four first-order derivatives of the horizontal wind). The U_x and V_y derivatives are derived from the horizontal divergence and the stretching deformation estimated by applying the SAVAD analysis to the two selected purls. A partial verification of the linearity condition for the U_y and V_x derivatives is also possible a posteriori comparing the two independent estimates of the shearing deformations performed with the two purls.

From Figs. 12c, 11a, and 11b representing the horizontal divergence and the stretching and shearing deformations, respectively, for the two purls, we can deduce that this linear assumption for the horizontal wind is quite well fullfilled. The differences that can be observed, in particular for the divergence, result from the fact that the first trajectory is performed in a zone of moderately convective precipitation, while the second one is in a region mixing stratiform and moderately convective precipitation. This explains in particular why the profile of horizontal divergence for the first trajectory is a little bit more convergent in the lower levels than for the second one. Moreover, it is important to note that there is 30 minutes between the two purls, during which the dynamics of the disturbance evolves. Nevertheless, these profiles remain in good agreement, which reasonably allows the application of the SAVAD and double SAVAD analyses.

We can notice that the profile of horizontal divergence is found to be very consistent with what has been previously deduced from studies on the stratiform regions (e.g., Figs. 6e and 7c of MH93 or Fig. 4c of ST86). This profile is characterized by a positive value below 2 km with a maximum 6×10^{-5} s^{-1} located at 1 km, a deep layer of convergence up to the 8-km altitude with the peak convergence just above the 0°C isotherm altitude (located at approximately 4.6 km), and a slight divergence above the 8-km altitude. The deep layer of convergence, like the divergence above, is in very good agreement with the flight-by-flight mean divergence profiles performed by MH95 using the TOGA COARE dataset (see their Figs. 4 and 5).

Nevertheless, it is to be noted that they found a slight low-level convergence, which characterizes young growing cumulonimbus towers, while we find a typical signature of more stratiform precipitation areas with a low-level divergence. This difference can be explained by the fact that they average convective and stratiform areas, while our profile is obtained on a more stratiform region. Our divergence profile is then logically more consistent with the stratiform divergence profiles previously produced by MH93 subdividing the MCSs in three types, that is, convective, stratiform, and intermediary.

The associated subsiding and ascending motions pre-

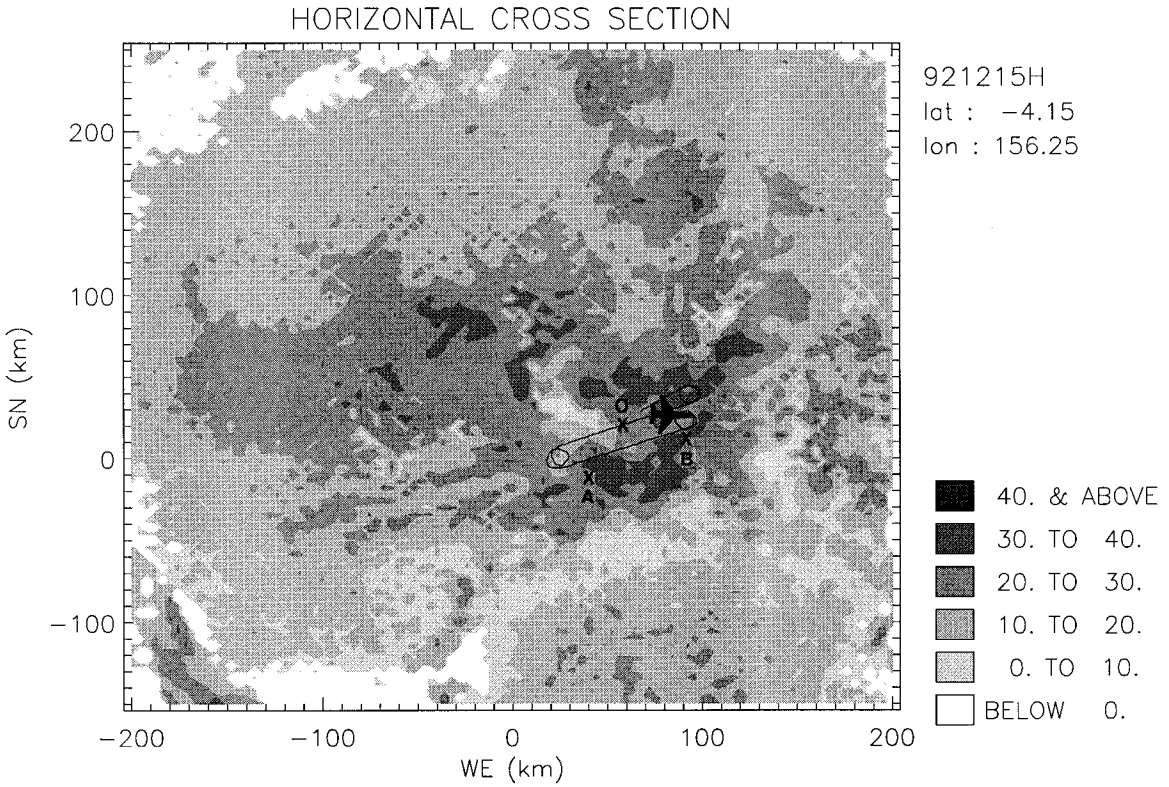

FIG. 10. Time-composite LF (lower fuselage radar) reflectivity map from 2025 to 2100 UTC 15 December 1992. Shaded contours are indicated on this figure. The black line is the flight track from the period of the time composite. The center of the domain is at 3.98°S, 156.77°E. Point *O* is located between the 2040 and 2055 UTC purls; *A* and *B* are the locations of the local MANDOP profiles of horizontal wind presented in Fig. 13.

sented in Fig. 12d are consistent, with a mesoscale downdraft below the 0°C isotherm altitude and with a mesoscale updraft with a maximum for the vertical velocity of 20–30 cm s^{-1} located near 8 km.

The vertical profiles of the mean fall velocity of the hydrometeors given in Fig. 11c clearly show this transition region between rain and snow located near the 0°C isotherm altitude, with values close to 6 m s^{-1} for the rain and 0.5 m s^{-1} for the snow. From this Fig. 11c, we notice that the two profiles are very close to each other for the rain area, below approximately 4 km. Nevertheless, for the ice phase below 7 km, some differences occur, which may be understood as different microphysical growth processes of the ice particles for both trajectories. Hence, further interpretation of these processes is carried out in the following.

In the ice region, the profiles of mean reflectivity (Fig. 11d) are nearly identical for both areas (the maximum difference is less than 1 dB*Z*). The fall velocity profile corresponding to the 2025 purl exhibits an increase of the fall speed, from 0.5 m s^{-1} at 7 km to 2.5 m s^{-1} at 5 km, which implies that the ice particles in this area tend to become heavier and probably more dense. The other profile at 2055 UTC is characterized by a constant value increasing only just above the 0°C isotherm altitude. A riming process between 5 and 7 km is then suspected for the 2025 UTC purl area, while there is no evidence of any active growth process for the other purl.

In order to illustrate and check this interpretation, an estimate of the mean reflectivity-weighted fall speed V_{tm} is carried out for two types of particles: graupel and ice aggregates. The analytical calculation leading to this estimate is briefly described in appendix C. For $Z = 20$ dB*Z*, which is the typical reflectivity value observed at the 6-km altitude in our profiles, the obtained fall speeds are

$$V_{tm}\ (\text{aggregates}) = 0.7\ \text{m s}^{-1}$$

$$V_{tm}\ (\text{graupel}) = 1.8\ \text{m s}^{-1}.$$

These results are very close to the values obtained at 6 km with the two purls. It may be then concluded in particular that the riming process was effectively active at 2025 UTC. The difference between the mean fall velocities for the two purls is in good agreement with the respective locations of these purls. This remark is reinforced by the structure of vertical air motions (Fig. 12d), showing more intense associated vertical motions in the 2025 UTC area (with a maximum of 30 cm s^{-1} at the 8-km altitude) than in the area sampled at 2055 UTC. Moreover, it is to be noted from this figure that the mesoscale downdraft is not initiated near the 0°C

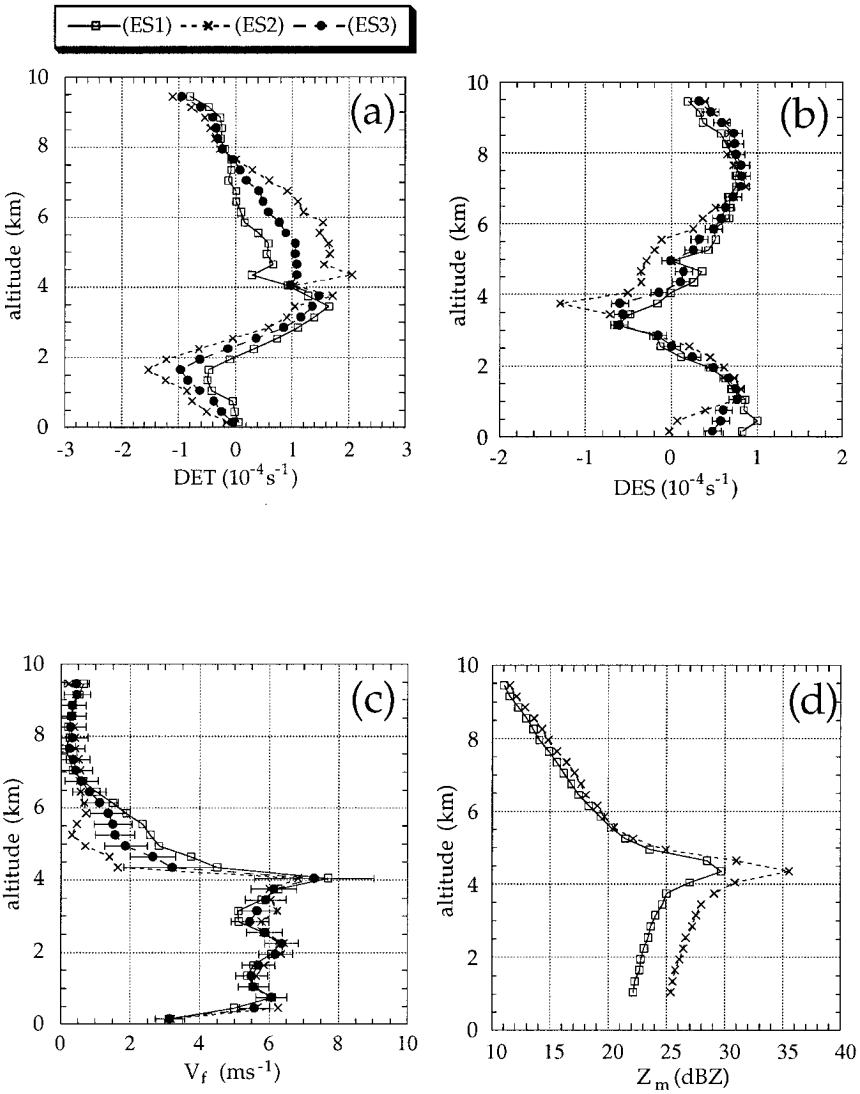

FIG. 11. Retrieval of (a) stretching deformation DET (10^{-4} s^{-1}), (b) shearing deformation DES (10^{-4} s^{-1}), and (c) terminal fall velocity (m s^{-1}) of the hydrometeors V_f by applying SAVAD at (ES1) 2025 and (ES2) 2055 UTC and double SAVAD to both trajectories (ES3). In (d) the mean reflectivity profiles Z_m (dBZ) deduced from the SAVAD analysis at (ES1) 2025 and (ES2) 2055 UTC are presented.

isotherm at 2025 UTC (which is the typical signature of a stratiform region, as shown for instance by the 2055 UTC profile given in Fig. 12d) but approximately 2 km below.

The transition region between ice and rain is well defined, with a bright band deduced from the profiles of mean reflectivity (Fig. 11d) located between 3.7 and 4.6 km. Note that the radiosoundings located far from the disturbance indicate a value of 4.3 km for the 0°C isotherm altitude, although the bright band indicates that the altitude of the 0°C isotherm is at 4.6 km within the sampled area. Since this latter value is deduced from an average within the MCS, it must be more representative of the inner environment of the disturbance. We will then take this 0°C isotherm altitude as a reference for the 15 December case study.

The peak value of 7.7 m s^{-1} observed at 4.05 km for the mean fall velocity of the hydrometeors must not be trusted since the associated error is much stronger at this level (1.7 m s^{-1}) than at other levels (approximately 0.4 m s^{-1}; see Fig. 11c). As explained at the end of section 3a, the error on V_f increases while the elevation angle decreases, which means that for the horizontal plane located at the altitude of the aircraft (4.1 km in this case), this error is maximized.

In the rain area, below 3.7 km, the profiles of mean reflectivity of Fig. 11d show a constant reflectivity gradient of 1 dBZ km^{-1} for both regions, indicating that

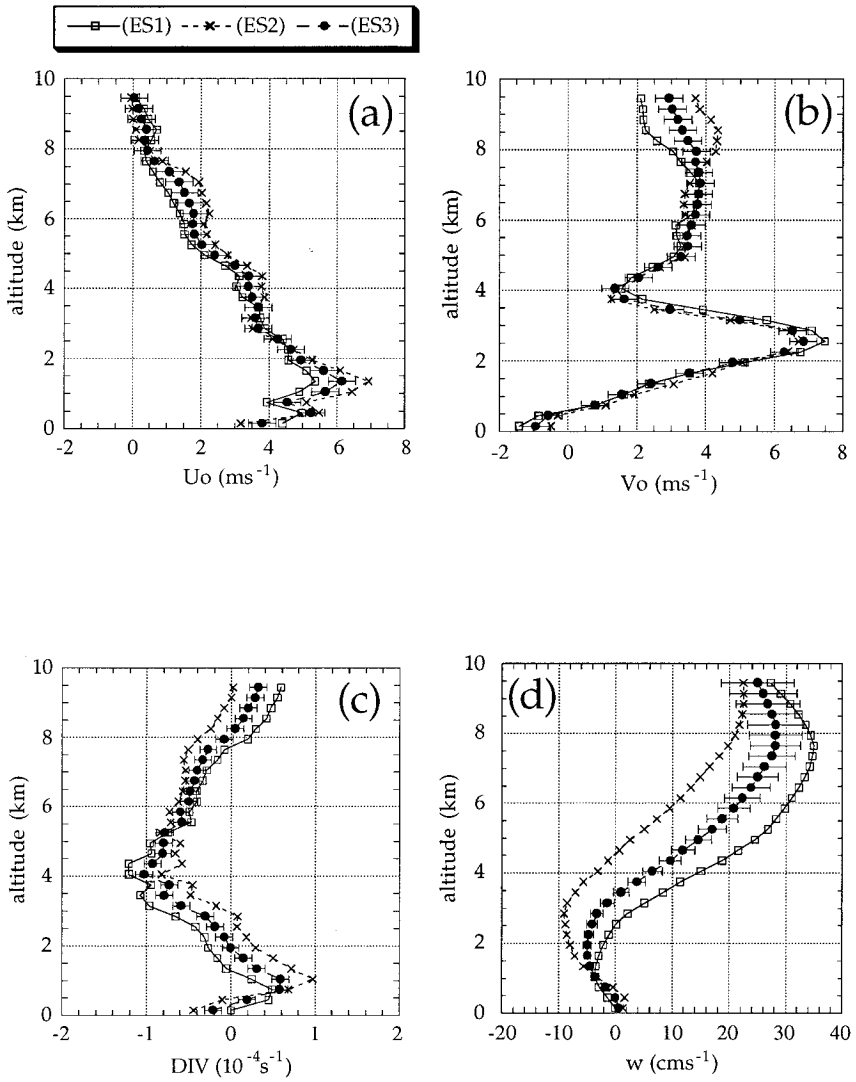

FIG. 12. Retrieval of (a) U_o (m s^{-1}), (b) V_o (m s^{-1}), (c) horizontal divergence DIV (10^{-4} s^{-1}), and (d) vertical air motion w (cm s^{-1}) by applying SAVAD at (ES1) 2025 AND (ES2) 2055 UTC and double SAVAD to both trajectories (ES3).

the evaporation process in unsaturated air is probably active. Nevertheless, we cannot conclude this definitely because of the oscillations observed in the profiles of terminal fall velocity. On the other hand, a systematic difference of 3 dBZ between the two curves is also observed on the reflectivity profiles. This difference can be explained. The average performed at 2025 UTC to obtain the mean reflectivity profile includes a large region of weak reflectivity on the western part, which tends to weaken the average. For the 2055 UTC purl, this region of weak reflectivity covers a smaller part of the sampled domain. The corresponding difference in the mean fall speed profiles of Fig. 11c is not very strong, even if the velocities corresponding to the 2025 UTC purl are effectively always smaller than for the 2055 UTC profile. We can show that this behavior is satisfying, by performing the previous analytical calculation of the mean reflectivity-weighted fall speed for the rain, at a given altitude of 2 km, corresponding to 23 and 26 dBZ, respectively, for the two curves (see appendix C). This calculation shows that the expected difference between the associated fall speeds is approximately 0.3 m s^{-1}, which is the order of magnitude of the error on this parameter.

Finally, we can see that a good correlation between the vertical profiles of mean fall velocity, vertical air motion, and mean reflectivity deduced from the SAVAD analysis is obtained. In particular, it evidences a riming process between 5 and 7 km for the 2025 UTC area that is not active in the 2055 UTC area.

The profiles of the horizontal components of the velocity U_o and V_o (Figs. 12a and 12b, respectively) show

the existence of a maximum located around the 2-km altitude. The lack of radiosoundings near the sampling zone at this time does not allow a direct validation of these profiles. Nevertheless, they can be compared to the flight-level measurements of the horizontal wind and to the profiles deduced from a three-dimensional wind field of the MANDOP analysis applied to the left part of the considered zone. This procedure allows to check the quality of the horizontal winds and first-order derived parameters, that is, DIV, DET, DES, and ROT obtained with the SAVAD analysis.

b. Application of double SAVAD and MANDOP on the 15 December 1992 MCS

The two purls at 2025 and 2055 UTC are now analyzed simultaneously using the double SAVAD analysis so as to separate the four first-order derivatives of the horizontal wind and rebuild the mesoscale vertical vorticity ROT (unreachable with the SAVAD analysis). Note that the double SAVAD profiles correspond to an average of the two SAVAD profiles weighted by the number of VAD circles used for the retrieval in each altitude layer. This point is illustrated by the profiles of horizontal mean wind, divergence, stretching and shearing deformations, and mean fall speed given in Figs. 11 and 12 (compare the curve corresponding to double SAVAD with the two associated SAVAD profiles). In order to validate the method, the obtained kinematic parameters are compared with those deduced from the three-dimensional wind field provided by MANDOP applied to the western part of the domain. An average of the horizontal wind deduced from MANDOP is carried out for each horizontal plane and presented in Figs. 13a,b. Also shown in these figures are the corresponding components of the horizontal mean wind deduced from the double SAVAD analysis.

We can notice that the same general tendencies are found for both components, even if some differences appear, especially for the V_o component. Nevertheless, one must recall that the horizontal wind retrieved by MANDOP is located in the western part of the domain sampled by the purls used for the application of the SAVAD analysis, which implies that we could not expect the components of the horizontal wind to be exactly similar. Moreover, the flight-level measurements of the horizontal wind (see Figs. 13a,b), averaged during the 2040 and 2055 UTC purls (respectively located on the western and eastern parts of the domain; see Fig. 10), indicate an important variation of the V_o component of the wind within the retrieval domain, which is in very good agreement with our retrieval.

Also presented in Figs. 13a,b are two local profiles deduced from the three-dimensional wind field performed by MANDOP (points *A* and *B* of Fig. 10). These profiles are taken from two grid points in regions exhibiting kinematically different structures. They clearly show that the U_o and V_o vertical profiles deduced from

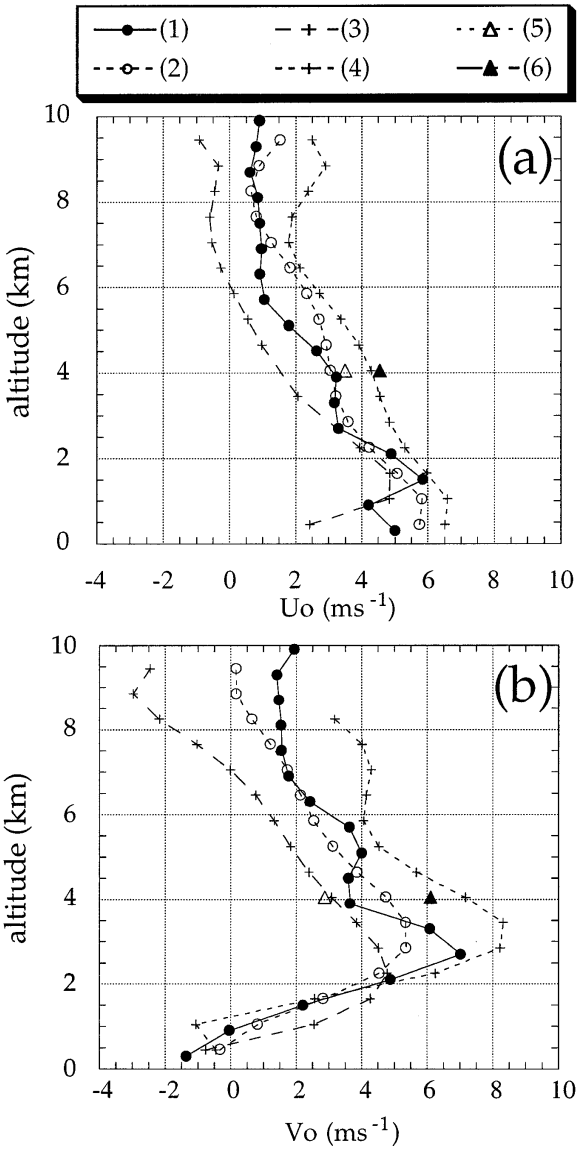

FIG. 13. Comparison of (a) U_o (m s^{-1}), (b) V_o (m s^{-1}) retrieved by the double SAVAD analysis (1), by MANDOP with a horizontal average for each horizontal plane denoted (2) and by MANDOP for two particular grid-point locations *A* and *B* defined in Fig. 10 [denoted (3) and (4)]. Also plotted are the flight level measurements of U_o and V_o averaged during the 2040 UTC purl (denoted 5) and 2055 UTC purl (denoted 6).

the two analyses are very consistent, even if (i) there is an important variation of the horizontal wind within the domain (as evidenced by the two local MANDOP profiles and the flight-level measurements) and (ii) the mean MANDOP profile is obtained on the left side of the SAVAD region.

The profile of the mesoscale vertical vorticity is also compared with the average performed on the three-dimensional MANDOP field (Fig. 14). The agreement between the two methods is not so satisfying, in particular at midlevels. These differences are probably due to the

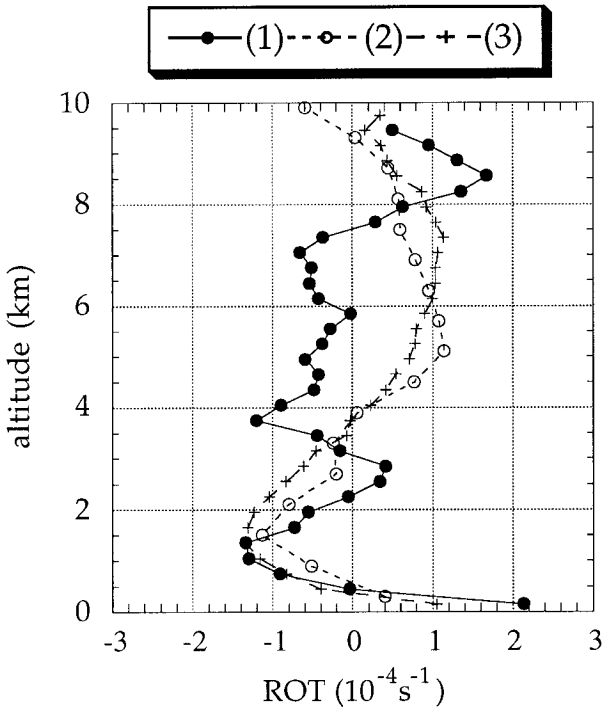

FIG. 14. Comparison of the mesoscale vertical vorticity ROT retrieved by the double SAVAD analysis applied to (1) the 2025 and 2055 UTC purls and (2) the 2040 and 2055 UTC purls, and by MANDOP with horizontal average for each horizontal plane (denoted 3). ROT is expressed in 10^{-4} s^{-1}.

fact that the two purls processed by the SAVAD analysis are too close spatially to each other to obtain an accurate estimate of the vorticity. In order to check this assumption, the purl at 2040 UTC (located on the left part of Fig. 10) and 2055 UTC are processed by the double SAVAD analysis. The 2040 UTC purl had not been previously chosen because the corresponding sampling was not a complete 360° circle, which reduced the number of measurements along the VAD circles. Moreover, this purl corresponds to a very different dynamic region, as shown by the local MANDOP profiles and the flight-level measurements presented in Fig. 13. Nevertheless, the profile of vertical vorticity deduced in this case is fairly consistent with the MANDOP analysis. A very good agreement (not shown herein) is also obtained for the other derivative terms DIV, DET, and DES.

c. Other attainable quantities

From the accurate estimate of the horizontal wind and its first-order derivatives, one can also retrieve other meteorological parameters of crucial importance such as the vertical profiles of the horizontal components of the pressure perturbation gradient (i.e., the pressure gradient force) and the temperature perturbation gradient using the following equations deduced from the equations of motion:

$$\frac{\partial p^*}{\partial x} = -\rho_0\left(\frac{\partial U}{\partial t} + U_0\frac{\partial U}{\partial x} + V_0\frac{\partial U}{\partial y} + W_0\frac{\partial U}{\partial z}\right) + \rho f V_0 \tag{30}$$

$$\frac{\partial p^*}{\partial y} = -\rho_0\left(\frac{\partial V}{\partial t} + U_0\frac{\partial V}{\partial x} + V_0\frac{\partial V}{\partial y} + W_0\frac{\partial V}{\partial z}\right) + \rho f U_0, \tag{31}$$

where p^* is the pressure perturbation (assuming a barotropic basic state), (U, V) is the linear horizontal wind retrieved by the double SAVAD analysis, (U_o,V_o) is the horizontal wind field at the location O defined in Fig. 10, ρ_0 is the reference for air density, f is the Coriolis parameter ($f = 2\omega \sin\phi$, where ω is the angular speed of the earth's rotation, ϕ is the latitude), and (x, y) are along the eastern and northern directions, respectively. This pressure perturbation gradient is estimated by evaluating these equations at the location $O(X_o, Y_o)$ defined in Fig. 10.

For this retrieval, we assume that the atmosphere is approximately in hydrostatic balance at the considered scale of motion, that is, mesoscale, when applying the SAVAD analysis on a stratiform or moderately convective precipitation area. This assumption has been checked using the results of the double SAVAD analysis, leading to $DW/Dt = \partial W/\partial t + U\partial W/\partial x + V\partial W/\partial y + W\partial W/\partial z \approx 1.3 \times 10^{-4}$ m s^{-2}. Hence, the gravitational term nearly balances the vertical component of the pressure gradient acceleration since both terms are much larger than the net vertical acceleration.

Once the pressure pertubation gradient is retrieved, the two horizontal components of the temperature gradient are calculated by differentiating with respect to z the two basic equations of horizontal motion and by using the equation of state of an ideal gas ($p = \rho RT$), which leads to the following equations:

$$\frac{\partial}{\partial z}\left(\frac{1}{\rho}\frac{\partial p}{\partial x}\right) = \frac{1}{\rho}\frac{\partial p}{\partial x}\frac{1}{T}\frac{\partial T}{\partial z} + \frac{g}{T}\frac{\partial T}{\partial x} \tag{32}$$

$$\frac{\partial}{\partial z}\left(\frac{1}{\rho}\frac{\partial p}{\partial y}\right) = \frac{1}{\rho}\frac{\partial p}{\partial y}\frac{1}{T}\frac{\partial T}{\partial z} + \frac{g}{T}\frac{\partial T}{\partial y}. \tag{33}$$

We can show that the first term on the right-hand side of these equations can be neglected with respect to the second term (less than 5%).

Finally, expressing these equations in terms of the temperature pertubation T^* (assuming a barotropic basic state), we obtain

$$\frac{\partial T^*}{\partial x} \approx \frac{T(z)}{g}\frac{\partial}{\partial z}\left(\frac{1}{\rho_0}\frac{\partial p^*}{\partial x}\right) \tag{34}$$

$$\frac{\partial T^*}{\partial y} \approx \frac{T(z)}{g}\frac{\partial}{\partial z}\left(\frac{1}{\rho_0}\frac{\partial p^*}{\partial y}\right), \tag{35}$$

where $T(z)$ is the real temperature as a function of the

altitude z. This temperature $T(z)$ is not available for 15 December in this area because of the lack of radiosoundings. It is thus estimated with a vertical profile of temperature taken at 1800 UTC and at the location (3.0°S, 156.0°E) deduced from the ECMWF model outputs for 15 December.

The first-order derivatives of the horizontal wind deduced from the 2040 and 2055 UTC purls processed by the double SAVAD are used to estimate these gradients $\delta p/\delta X$ and $\delta p/\delta Y$ in a frame (X, Y), with X in the along-line direction from the left to the right part of the disturbance, and Y in the cross-line direction oriented from front to rear.

The point $(X_o, Y_o) = (0, 0)$ is located in the southeastern part of the MCS (noted O in Fig. 10), between the 2040 and 2055 UTC purls, at the frontside of the convective area, just behind the gust front (see Fig. 10). The vertical profiles of the cross-line components of the pressure and temperature perturbation gradients are presented in Figs. 15a and 15b, respectively. The cross-line pressure perturbation gradient is characterized by a slight positive value below the 1-km altitude, a strong negative value between the 1- and 3.5-km altitudes with a peak value of -2×10^{-3} Pa m^{-1} (which represents approximately a 0.2-mb variation for 10 km), and a positive value above 3.5 km with two peak values located at the 4- and 8-km altitudes. This evidences the existence of a slight pressure increase associated with the gust front in the low levels and the well-known pressure low in the stratiform region near 700-mb level (see for instance LeMone et al. 1984).

This vertical profile can be compared with a two-dimensional numerical simulation of a mesoscale convective system performed by Szeto and Cho (1994). They found the same vertical variations and order of magnitude of the cross-line pressure perturbation (see in particular their Fig. 9b) at the point $X = 5$ located approximately as our point of reference (0, 0) relatively to the gust front.

The cross-line temperature perturbation gradient presented in Fig. 15b exhibits a negative variation from front to rear up to 3 km in altitude. This indicates that the air coming at low levels from the stratiform part of the system is much colder than the airflow coming from ahead of the disturbance. This result is a classical thermodynamic feature of the tropical squall lines (see for instance Roux and Ju 1990, Fig. 10a; Hauser et al. 1988, Fig. 3d; and others).

The peak negative value of -7×10^{-5} K m^{-1} is located at the 1-km altitude, which represents a variation of ± 0.7 K each 10 km from our point of reference.

A strong positive temperature perturbation gradient is located just below the 0°C isotherm altitude, overlayed by a strong negative gradient within the melting layer. Above this level, the gradient is close to 0, considering the accuracy of the retrieval (slightly positive up to the 8-km altitude, slightly negative above). The same features for the temperature perturbation are also observed in the temperature field of Szeto and Cho (1994) at the same location $X = 5$ (see their Fig. 7b).

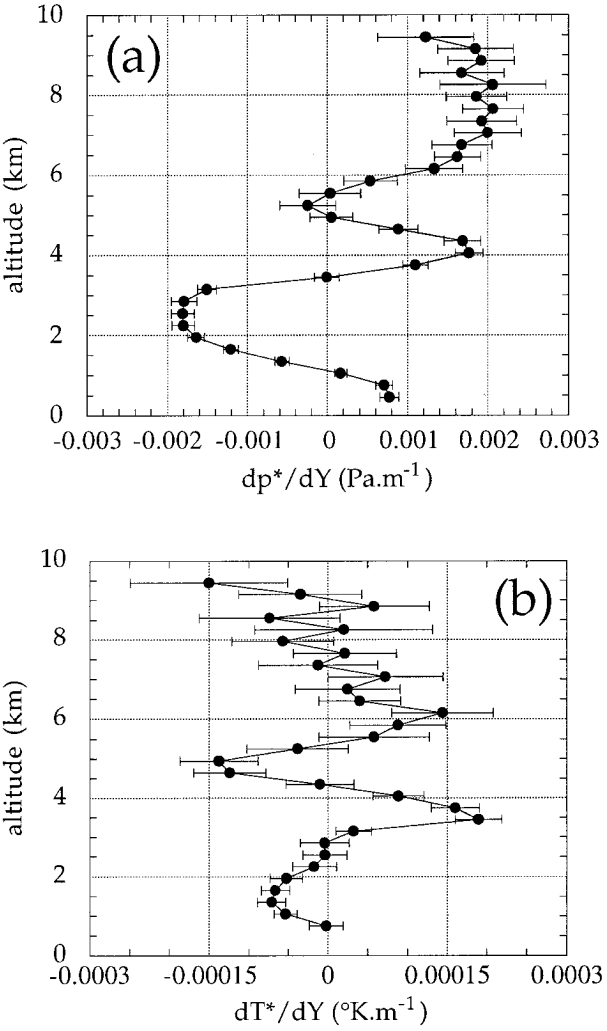

FIG. 15. Vertical profiles of (a) the cross-line pressure perturbation gradient $\delta p^*/\delta Y$ (Pa m^{-1}), and (b) the cross-line temperature perturbation gradient $\delta T^*/\delta Y$ (K m^{-1}), retrieved by the double SAVAD analysis.

The retrieval of these gradients is an illustration of the possible applications that can be developed using the wind field and its derivatives obtained by the double SAVAD analysis. Note that other derived quantities, essential (i) to infer the mesoscale processes implied in the initiation, evolution, and organization of mesoscale convective systems and (ii) to validate parameterization (such as the momentum, heat, and moisture budgets), can be accurately estimated using the SAVAD and double SAVAD approaches.

5. Possible extension of the SAVAD analysis

In the case of a dual-beam radar, the γ angle, defined in Fig. 3 as the elevation of the Doppler radial from the

plane perpendicular to the track, is not negligible (18.5° for the ELDORA–ASTRAIA system). Rewriting (11) without neglecting the x angle leads to the following ρ_h quadratic form:

$$\frac{a_0}{2\sin\alpha} = -\frac{\mathrm{DIV}}{2h}\rho_h^2 - \frac{R_c}{2h}(\mathrm{DIV}\cos x + \mathrm{ROT}\sin x)\rho_h + V_f. \quad (36)$$

Using a quadratic regression leads then to the three following coefficients:

$$C_1 = -\frac{\mathrm{DIV}}{2h},$$

$$C_2 = -\frac{R_c}{2h}(\mathrm{DIV}\cos x + \mathrm{ROT}\sin x),$$

$$C_3 = V_f. \quad (37)$$

DIV is obtained here by the determination of C_1, and C_2 includes an extra term depending on the mesoscale vertical vorticity ROT, which can be retrieved by combining C_1 and C_2. This extension of the SAVAD analysis can be applied separately to data collected by either the fore antenna or the aft antenna of a dual-beam airborne Doppler radar leading to two estimates of these parameters. Note, however, that, as explained previously, DIV is less precisely determined in this quadratic approach than in the case of the proposed linear approach. Moreover, the vertical vorticity ROT is affected by strong errors due to the fact that its contribution to the C_2 term is weak (for the typical x value of 20°).

This procedure will be applied in the future by processing separately the fore and aft scannings performed by the P3-43 and ELDORA–ASTRAIA dual-beam airborne radars that operated during TOGA-COARE.

6. Conclusions

In this paper, the SAVAD approach, devoted to the processing of airborne radar observations from a single-beam antenna scanning perpendicular to the track of an aircraft flying a circular path, has been described. This analysis has been tested through different simulations and validated using real airborne Doppler radar data collected during TOGA COARE.

This analysis provides the horizontal mean wind, its horizontal divergence, its stretching and shearing deformations, and the mean fall velocity of the hydrometeors in each altitude slice. Moreover, combining two observations deduced from successive purls in the double SAVAD analysis (equivalent to the double VAD analysis that was operational for ground-based radars), one can separate all the first-order derivatives of the horizontal wind that are used to rebuild the mesoscale vertical vorticity and the complete three-dimensional wind field.

Hence, it is possible to follow the evolution of these parameters during the MCSs lifetimes by applying those two previous methodologies on all the couples of purls performed by the aircraft in the precipitating system. This procedure allows us to calculate the associated mesoscale processes responsible for this evolution. This work will be done in the future using the TOGA COARE database for selected case studies characterized by strong time evolution.

As explained in section 2b(1), the restrictions concerning the applicability of these methods, that is, a single-beam antenna performing track-perpendicular scannings during circular trajectories, can be overcome by performing a quadratic regression instead of a linear one, in order to extract kinematic parameters from dual-beam antennae, such as the NOAA P3-43 and ELDORA–ASTRAIA systems. In this case, the modified analyses are applied separately to data collected by either the fore antenna or the aft antenna. On the other hand, a new methodology devoted to the retrieval of kinematic parameters from dual-beam airborne radar data, which allows processing data from both antennae at the same time, is presently under progress.

Acknowledgments. The TOGA COARE experiment is the result of a cooperative work involving several countries. In addition to the contribution of the participating institutes, financial support was provided by the Institut National des Sciences de 1'Univers. Special recognition must be made to Dr. Virginie Marécal for her helpful comments.

APPENDIX A

Description of the Preprocessing of the Airborne Doppler Radar Data Used in the SAVAD Analysis

The different effects that have to be corrected during the preprocessing of the airborne Doppler radar data can be summarized as follows:

1) the echo returned from the earth's surface,
2) the ground-relative velocity of the aircraft,
3) the GPS corrections of positioning and aircraft speed,
4) the aliased velocities, and
5) the apparent antenna motion.

The contribution of the echo returned from the earth's surface is eliminated by calculating which gates contain the reflectivity of the ground in their sampling volumes.

Recent studies have shown that this ground echo could also be used to estimate errors in navigation and radar pointing angles (Testud et al. 1995). These corrections have been included in the preprocessing, as well as the corrections of position and ground-relative velocity of the aircraft using the Global Positioning System (GPS).

Since the sum of the aircraft speed and the radial

velocity is aliased and recorded for each gate, we have also removed this contribution by simply subtracting from the radial velocity the projection of the ground-relative velocity of the aircraft.

The unfolding process of the radial velocities consists of a continuity test, comparing the current gate with a mean of the 10 preceding gates and also with the same gate from the preceding ray. The gate is eliminated if the difference is greater than a fixed threshold (9 m s^{-1}). This process is initialized with the value of the radial wind at the radar location deduced from the wind speed measured by a sensor located on the aircraft.

The last correction carried out is the removal of the additional apparent antenna motion (Lee et al. 1994) that appears when the pitch and heading angles of the aircraft are changing with time and the Inertial Navigation System (INS) is located some distance L away from the antenna. This apparent antenna motion V_a is

$$V_a = -L\left\{i\left[\cos H(1+\cos P)\frac{dH}{dt} - \sin P \sin H\frac{dP}{dt}\right] - j\left[\sin H(1+\cos P)\frac{dH}{dt} + \sin P\cos H\frac{dP}{dt}\right] + k\cos P\frac{dP}{dt}\right\}, \quad \text{(A1)}$$

where H is the heading, P is the pitch, (i, j, k) is the earth-relative coordinate system, and L is the INS–antenna distance (L = 29.8 m for the ELDORA–ASTRAIA system, L = 25.4 m for both P3 systems).

The effect of the apparent antenna motion is negligible for a straight-line pattern but cannot be ignored when the aircraft is turning, which is the case here. In fact, the maximum value for the apparent antenna motion obtained in the TOGA COARE purls was approximately 1.5 m s^{-1}.

APPENDIX B

Description of the Numerical Tests

In all the simulations described in appendix B, the horizontal wind (U, V) is obtained through (1) and (2) and projected on simulated rays for each couple (elevation α, azimuth β) through

$$V_r(\alpha, \beta) \approx -U\sin\beta\cos\alpha - V\cos\beta\cos\alpha + V_t\sin\alpha, \quad \text{(B1)}$$

where V_t is the mean fall velocity of the hydrometeors, positive downward.

The simulation type I is constructed as follows:

$$U_o = 10 \text{ m s}^{-1}; \qquad V_o = 5 \text{ m s}^{-1}$$
$$U_x = 2\times10^{-5} \text{ s}^{-1}; \qquad U_y = -1\times10^{-5} \text{ s}^{-1}$$
$$V_x = 1\times10^{-5} \text{ s}^{-1}; \qquad V_y = 1\times10^{-5} \text{ s}^{-1},$$

that is,

$$\text{DIV} = 3\times10^{-5} \text{ s}^{-1}; \qquad \text{DET} = 1\times10^{-5} \text{ s}^{-1};$$
$$\text{DES} = 0.$$

Let us notice that this wind field does not change with altitude in order to check if the obtained errors depend on the considered elevation angle.

In order to test the performance of the SAVAD analysis when a little quadratic component is added to the horizontal wind (simulation type II), we have rewritten (1) under the following form:

$$U = U_o + U_x(X - X_o) + U_{xx}(X - X_o)^2 \quad U_{yy}(Y - Y_o)^2,$$

where U_{xx} and U_{yy} are the second-order derivatives of the U component of the horizontal wind with respect to x and y, respectively.

The other characteristics of the wind of this simulation type II are

$$U_o = 10 \text{ m s}^{-1}; \qquad V_o = 5 \text{ m s}^{-1}$$
$$U_x = 2\times10^{-4} \text{ s}^{-1}; \qquad U_y = -1\times10^{-4} \text{ s}^{-1}$$
$$V_x = 1\times10^{-4} \text{ s}^{-1}; \qquad V_y = 1\times10^{-4} \text{ s}^{-1},$$

that is,

$$\text{DIV} = 3\times10^{-4} \text{ s}^{-1}; \qquad \text{DET} = 1\times10^{-4} \text{ s}^{-1};$$
$$\text{DES} = 0.$$

For the simulation type III, which is carried out to test the applicability of the double VAD analysis, these parameters are chosen as functions of altitude:

$$U_1 = 0.8z - 6, \qquad V_1 = 8\sin\left(\frac{\pi}{10}z\right)$$
$$U_2 = U_1 + U_xX_{12} + U_yY_{12},$$
$$V_2 = V_1 + V_xX_{12} + V_yY_{12}$$
$$U_x = 0.3\times10^{-4}\cos\left(\frac{2\pi}{14}z + \frac{\pi}{14}\right),$$
$$U_y = -0.3\times10^{-4}\sin\left(\frac{\pi}{10}z\right)$$
$$V_x = 0.7\times10^{-4}\sin\left(\frac{\pi}{10}z\right),$$
$$V_y = 0.7\times10^{-4}\cos\left(\frac{2\pi}{14}z + \frac{\pi}{14}\right).$$

Terms (U_1, V_1) and (U_2, V_2) are the horizontal wind at the location of the center of the first purl and second purl, respectively.

The simulation type IV uses the following coefficients:

$$U_o = 0.8z - 6, \qquad V_o = 16 \sin\left(\frac{\pi}{10}z\right) - 2$$

$$\text{DIV} = 1 \times 10^{-4} \cos\left(\frac{2\pi}{14}z + \frac{\pi}{14}\right),$$

$$\text{DET} = -0.4 \times 10^{-4} \cos\left(\frac{2\pi}{14}z + \frac{\pi}{14}\right)$$

$$\text{DES} = 0.4 \times 10^{-4} \sin\left(\frac{\pi}{10}z\right).$$

The values of DIV, DET, and DES are simply recomputed from the first-order derivatives of the simulation type III.

APPENDIX C

Analytical Calculation of the Mean Reflectivity-Weighted Fall Speed V_{tm} as a Function of the Reflectivity Z

The analytical calculation of $V_{tm} = f(Z)$ is described in the following. For this purpose, it is to be noted that a Marshall–Palmer distribution is considered for both (V_{tm}, Z) and that the Rayleigh approximation is assumed for Z, which leads to

$$V_{tm} = \frac{\int_D N(D)v(D)D^3\, dD}{\int_D N(D)D^3\, dD} f(h) \qquad \text{(C1)}$$

$$Z = \int_D N(D)D^6\, dD, \qquad \text{(C2)}$$

with $N(D) = N_0 \exp(-\lambda D)$ and $N_0 = 8 \times 10^6$ m^{-4}, where Z (mm^6 m^{-3}) is the reflectivity, $f(h) = (\rho_0/\rho)^{0.4}$ is a correcting factor as a function of the altitude h, ρ is the air density, ρ_0 is the air density at ground level, D is the diameter of a given particle, $m(D)$ is the mass, $v(D)$ is the terminal fall velocity of a particle with diameter D, and $N(D)$ is the number of particles per unit volume of air with diameter D to $D + dD$.

Let us notice also that the relation $v(D)$ used in the calculation is from Locatelli and Hobbs (1974). This leads to the following relationships:

for graupel, $V_{tm} = 1.0672Z^{0.0529}f(h)$;

for ice aggregates, $V_{tm} = 0.4801Z^{0.0157}f(h)$.

With a typical value of $Z = 20$ dBZ at the 6-km altitude, deduced from our Fig. 11d, the values of the reflectivity-weighted fall velocity are

$$V_{tm}(\text{aggregates}) = 0.7 \text{ m s}^{-1}$$

$$V_{tm}(\text{graupel}) = 1.8 \text{ m s}^{-1}.$$

For the rain areas, the relation $V_{tm} = 2.864Z^{0.0714}f(h)$ is used to explain the systematic difference between the two profiles of terminal fall velocity in the rain region (see Fig. 11c). At a given altitude of 2 km, the corresponding profiles of mean reflectivity (Fig. 11d) are characterized by mean values of 23 and 26 dBZ, respectively, for the 2025 and 2055 UTC purls. The analytical calculation of the reflectivity-weighted fall velocity for these two values of reflectivity gives

$$V_{tm}(23 \text{ dBZ}) = 4.68 \text{ m s}^{-1}$$

$$V_{tm}(26 \text{ dBZ}) = 4.96 \text{ m s}^{-1},$$

which indicates approximately a 0.3 m s^{-1} difference in terms of fall velocity.

REFERENCES

Breger, G., 1977: Etude par radar Doppler des mouvements atmosphériques au voisinage d'un front froid. Thèse de 3ème cycle, Université Pierre et Marie Curie Paris VI, 108 pp. [Available from University Paris VI, 2 Place Jussieu, 75006 Paris, France.]

Browning, K. A., and R. Wexler, 1968: The determination of kinematic properties of a wind field using Doppler radar. *J. Appl. Meteor.*, **7,** 105–113.

Chong, M., P. Amayenc, G. Scialom, and J. Testud, 1987: A tropical squall line observed during the COPT 81 experiment in West Africa. Part I: Kinematic structure inferred from dual-Doppler radar data. *Mon. Wea. Rev.*, **115,** 670–694.

Gamache, J. F., and R. A. Houze Jr., 1983: Water budget of a mesoscale convective system in the tropics. *J. Atmos. Sci.*, **40,** 1835–1850.

Hauser, D., F. Roux, and P. Amayenc, 1988: Comparison of two methods for the retrieval of the thermodynamic and microphysical variables from Doppler radar measurements: Application to the case of a tropical squall line. *J. Atmos. Sci.*, **45,** 1285–1303.

Hertenstein, R. F. A., and W. A. Schubert, 1991: Potential vorticity anomalies associated with squall lines. *Mon. Wea. Rev.*, **119,** 1663–1672.

Hildebrand, P. H., and C. K. Mueller, 1985: Evaluation of meteorological airborne Doppler radar. Part I: Dual-Doppler analyses of air motions. *J. Atmos. Oceanic Technol.*, **2,** 362–380.

——, C. A. Walther, C. Frush, J. Testud, and G. Baudin, 1995: The ELDORA/ASTRAIA airborne Doppler weather radar: Goals, design and first field tests. *Proc. IEEE*, **82,** 1873–1890.

Jorgensen, D. P., P. H. Hildebrand, and C. L. Frush, 1983: Feasability test of an airborne pulse-Doppler meteorological radar. *J. Climate Appl. Meteor.*, **22,** 744–757.

Lee, W.-C., P. Dodge, F. D. Marks, and P. H. Hildebrand, 1994: Mapping of airborne Doppler radar data. *J. Atmos. Oceanic Technol.*, **11,** 572–578.

LeMone, M. A., G. M. Barnes, and E. J. Zipser, 1984: Momentum flux by lines of cumulonimbus over the tropical oceans. *J. Atmos. Sci.*, **41,** 1914–1932.

Lhermitte, R. M., and D. Atlas, 1961: Precipitation motion by pulse Doppler radar. Preprints, *Ninth Weather Radar Conf.*, Boston, MA, Amer. Meteor. Soc., 218–223.

Locatelli, J. D., and P. V. Hobbs, 1974: Fallspeeds and masses of solid precipitation particles. *J. Geophys. Res.*, **79,** 2185–2197.

Mapes, B. E., and R. A. Houze Jr., 1993: An integrated view of the

1987 Australian monsoon and its mesoscale convective systems. Part II: Vertical structure. *Quart. J. Roy. Meteor. Soc.,* **119,** 733–754.

——, and ——, 1995: Diabatic divergence profiles in western Pacific mesoscale convective systems. *J. Atmos. Sci.,* **52,** 1807–1828.

Matejka, T. J., and R. C. Srivastava, 1981: Doppler radar study of a region of widespread precipitation trailing a mid-latitude squall-line. Preprints, *20th Conf. on Radar Meteor.,* Boston, MA, Amer. Meteor. Soc., 353–357.

Roux, F., and S. Ju, 1990: Single-Doppler observation of a West African squall line on 27–28 May 1981 during COPT 81: Kinematics, thermodynamics and water budget. *Mon. Wea. Rev.,* **118,** 1826–1854.

Scialom, G., and J. Testud, 1986: Retrieval of horizontal wind field and mesoscale vertical vorticity in stratiform precipitation by conical scannings with two Doppler radars. *J. Atmos. Oceanic Technol.,* **3,** 693–703.

——, and Y. Lemaître, 1990: A new analysis for the retrieval of the three-dimensional wind field from multiple Doppler radars. *J. Atmos. Oceanic Technol.,* **7,** 640–665.

——, and ——, 1994: QVAD: A method to obtain quadratic winds from conical scans by a Doppler weather radar network. *J. Atmos. Oceanic Technol.,* **11,** 909–926.

Smull, B. F., and R. A. Houze Jr., 1985: A midlatitude squall line with a trailing region of stratiform rain: Radar and satellite observations. *Mon. Wea. Rev.,* **113,** 117–133.

Srivastava, R. C., T. J. Matejka, and T. J. Lorello, 1986: Doppler radar study of the trailing anvil region associated with a squall line. *J. Atmos. Sci.,* **43,** 356–377.

Szeto, K. K., and H. R. Cho, 1994: A numerical investigation of squall lines. Part I: The control experiment. *J. Atmos. Sci.,* **51,** 414–424.

Testud, J., G. Breger, P. Amayenc, M. Chong, B. Nutten, and A. Sauvaget, 1980: A Doppler radar observation of a cold front. Three dimensional air circulation, related precipitation system and associated wave-like motions. *J. Atmos. Sci.,* **37,** 78–98.

——, P. H. Hildebrand, and W.-C. Lee, 1995: A procedure to correct airborne Doppler radar data for navigation errors, using the echo returned from the earth's surface. *J. Atmos. Oceanic Technol.,* **12,** 799–820.

Webster, P. J., and R. Lukas, 1992: The Coupled Ocean–Atmosphere Response Experiment. *Bull. Amer. Meteor. Soc.,* **73,** 1377–1415.

Zipser, E. J., 1977: Mesoscale and convective-scale downdrafts as distinct components of squall line structure. *Mon. Wea. Rev.,* **105,** 1568–1589.